

A Mononuclear Nonheme Iron(IV)-Oxo Complex of a Substituted N4Py Ligand: Effect of Ligand Field on Oxygen Atom Transfer and C–H Bond Cleavage Reactivity

Reena Singh,^{*,†} Gaurab Ganguly,[†] Sergey O. Malinkin,^{‡,||} Serhiy Demeshko,[§] Franc Meyer,^{§,||} Ebbe Nordlander,[‡] and Tapan Kanti Paine^{*,†,||}

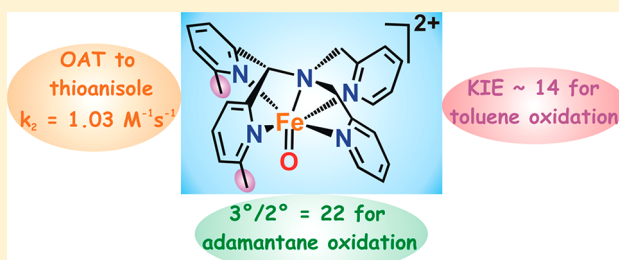
[†]School of Chemical Sciences, Indian Association for the Cultivation of Science, 2A & 2B Raja S. C. Mullick Road, Jadavpur, Kolkata 700032, India

[‡]Chemical Physics, Department of Chemistry, Lund University, Box 124, SE-22100 Lund, Sweden

[§]Universität Göttingen, Institut für Anorganische Chemie, Tammanstrasse 4, D-37077 Göttingen, Germany

Supporting Information

ABSTRACT: A mononuclear iron(II) complex $[\text{Fe}^{\text{II}}(\text{N4Py}^{\text{Me2}})(\text{OTf})](\text{OTf})(\mathbf{1})$, supported by a new pentadentate ligand, bis(6-methylpyridin-2-yl)-*N,N*-bis((pyridin-2-yl)methyl)methanamine (N4Py^{Me2}), has been isolated and characterized. Introduction of methyl groups in the 6-position of two pyridine rings makes the N4Py^{Me2} a weaker field ligand compared to the parent N4Py ligand. Complex $\mathbf{1}$ is high-spin in the solid state and converts to $[\text{Fe}^{\text{II}}(\text{N4Py}^{\text{Me2}})(\text{CH}_3\text{CN})](\text{OTf})_2$ ($\mathbf{1a}$) in acetonitrile solution. The iron(II) complex in acetonitrile displays temperature-dependent spin-crossover behavior over a wide range of temperature. In its reaction with *m*-CPBA or oxone in acetonitrile at -10 °C, the iron(II) complex converts to an iron(IV)-oxo species, $[\text{Fe}^{\text{IV}}(\text{O})(\text{N4Py}^{\text{Me2}})]^{2+}$ ($\mathbf{2}$). Complex $\mathbf{2}$ exhibits the Mössbauer parameters $\delta = 0.05$ mm/s and $\Delta E_{\text{Q}} = 0.62$ mm/s, typical of N-ligated $S = 1$ iron(IV)-oxo species. The iron(IV)-oxo complex has a half-life of only 14 min at 25 °C and is reactive toward oxygen-atom-transfer and hydrogen-atom-transfer (HAT) reactions. Compared to the parent complex $[\text{Fe}^{\text{IV}}(\text{O})(\text{N4Py})]^{2+}$, $\mathbf{2}$ is more reactive in oxidizing thioanisole and oxygenates the C–H bonds of aliphatic substrates including that of cyclohexane. The enhanced reactivity of $\mathbf{2}$ toward cyclohexane results from the involvement of the $S = 2$ transition state in the HAT pathway and a lower triplet-quintet splitting compared to $[\text{Fe}^{\text{IV}}(\text{O})(\text{N4Py})]^{2+}$, as supported by DFT calculations. The second-order rate constants for HAT by $\mathbf{2}$ is well correlated with the C–H bond dissociation energies of aliphatic substrates. Surprisingly, the slope of this correlation is different from that of $[\text{Fe}^{\text{IV}}(\text{O})(\text{N4Py})]^{2+}$, and $\mathbf{2}$ is more reactive only in the case of strong C–H bonds (>86 kcal/mol), but less reactive in the case of weaker C–H bonds. Using oxone as the oxidant, the iron(II) complex displays catalytic oxidations of substrates with low activity but with good selectivity.

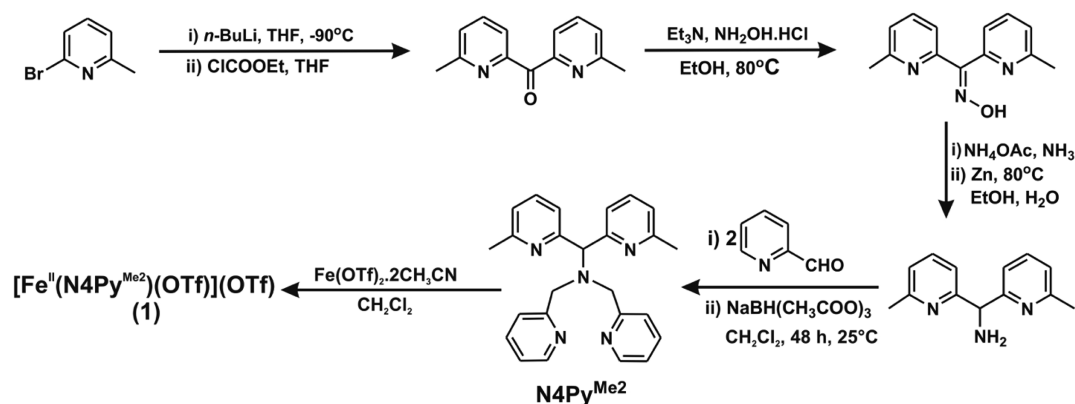


INTRODUCTION

A large variety of iron enzymes activate dioxygen (O_2) to catalyze biologically important oxidation reactions.^{1–5} For many of these oxidation reactions, the reductive activation of dioxygen at the reduced iron center leads to the generation of high-valent iron-oxo species as the active oxidant. In heme biochemistry, high-valent iron(IV)-oxo species coupled to a radical (e.g., iron(IV)-oxo(porphyrin radical cation)) have been identified as active oxidants.^{6–8} Diiron(IV) intermediates, generated from dinuclear nonheme iron enzymes, have been postulated to have strong oxidizing power, permitting them to cleave strong hydrocarbon C–H bonds.^{1,9–12} The characterization of high-spin nonheme iron(IV)-oxo intermediates in taurine α -ketoglutarate dioxygenase (TauD) and in other nonheme iron oxygenases such as prolyl hydroxylase, tyrosine hydroxylases, and in halogenases^{13–19} has fueled interest in synthesis and reactivity studies of nonheme high-valent iron-oxo complexes.^{20–29} Consequently, many mononuclear non-

heme iron(IV)-oxo complexes supported by polydentate ligands have been reported over the last couple of decades.^{22,23,25,30,31} These complexes display varying degrees of stability and exhibit versatile reactivity such as C–H bond activation and oxo-atom-transfer reactions. The iron(IV)-oxo complex supported by the 1,4,8,11-tetramethyl-1,4,8,11-tetraazacyclotetradecene (TMC) ligand can only oxidize substrates with C–H bond dissociation energies (BDEs) <80 kcal/mol; whereas those based on N4Py ($\text{N4Py} = N,N$ -bis(2-pyridylmethyl)-*N*-bis(2-pyridyl)methylamine), Bn-tpen (Bn-tpen = *N*-benzyl-*N,N,N'*-tris(2-pyridylmethyl)-1,2-diaminoethane), and Me_3NTB (tris(*N*-methylbenzimidazol-2-yl)-methylamine) have been reported to oxidize C–H bonds as strong as those of cyclohexane (C–H BDE 99.3 kcal/mol).^{32–36} While enzymatic systems involve high-spin ($S =$

Received: September 11, 2018

Scheme 1. Synthesis of the N4Py^{Me2} Ligand and Its Iron(II) Complex

2) iron(IV)-oxo oxidants, the majority of the well-characterized iron(IV)-oxo complexes possess an $S = 1$ ground spin state.^{20,21,24,25,27,31,36–51} Recently, the isolation and reactivity studies of a few high-spin iron(IV)-oxo complexes have been reported.^{52–60} Theoretical calculations suggest that $S = 2$ iron(IV)-oxo species are more reactive toward C–H bond activation than the $S = 1$ species,^{61,62} which would be an obvious reason for the presence of the $S = 2$ spin state in intermediates for both mononuclear and dinuclear nonheme enzyme sites in contrast to the low-spin form that is found in heme enzymes. To stabilize high-spin iron(IV)-oxo complexes, weak field ligands are required. The supporting ligands should either enforce C_{4v} symmetry with weak equatorial donors or should engender C_{3v} symmetry to enable high-spin configuration.²⁴ Furthermore, appropriate design of the supporting ligand is required to tune the stability and reactivity of the resulting iron-oxo complexes.

The $S = 1$ iron(IV)-oxo complex of the N4Py ligand has been reported to exhibit C–H bond activation and oxo-atom-transfer reactivity.³⁸ In spite of its long half-life (60 h at 298 K), the complex can slowly oxidize the C–H bonds of cyclohexane. Computational modeling indicates that a small energy gap between the $S = 1$ and $S = 2$ states enables the complex to react via the accessible $S = 2$ state.⁶² If the energy gap between the two states can be reduced by tuning the supporting ligand, the more easily accessible $S = 2$ state is predicted to make an iron(IV)-oxo species highly reactive. A pentadentate ligand based on the N4Py platform incorporating phenyl substituents on the dipyriddy unit has been reported to decrease the energy separation between the $S = 1$ and $S = 2$ states compared to that for the parent N4Py system.⁶³ However, due to the orientation of the phenyl rings in close proximity to the iron-oxo units, the intermediate was prone to intramolecular aromatic C–H hydroxylation. Substitution of phenyl groups on the pyridine rings by 2,6-difluorophenyl groups allowed the trapping of the corresponding $S = 1$ iron(IV)-oxo complex for structural characterization. Interestingly, the iron(IV)-oxo species was capable of carrying out intramolecular aromatic C–F bond hydroxylation.^{64,65} Replacement of the two pyridine donors of the bis(pyridyl-2-methyl)arms of the N4Py scaffold by *N*-methylbenzimidazole or quinoline groups has been reported to enhance the reactivity of the corresponding iron(IV)-oxo complexes toward hydrogen-atom and oxygen-atom-transfer reactions.^{66,67} Very recently, the X-ray crystal structures of the iron(IV)-oxo complexes of the N4Py-type ligands with two *N*-methylbenzi-

midazole or quinoline donors revealed longer average Fe–N distances than those of the corresponding complex of the parent N4Py ligand. The steric effects of the quinolyl donors not only increased the average Fe–N bond length but also tilted the Fe=O unit away from the donor groups.⁶⁷ With an objective to develop highly reactive iron-oxo complexes, we have been exploring the effect of alkyl substitution on the pyridine donors of the N4Py ligand on the reactivity and stability of the corresponding iron(IV)-oxo complexes. We report herein the synthesis and characterization of a mononuclear iron(II) complex $[\text{Fe}^{\text{II}}(\text{N4Py}^{\text{Me2}})(\text{OTf})](\text{OTf})$ (**1**), supported by the new bis(6-methylpyridin-2-yl)-*N,N*-bis((pyridin-2-yl)methyl)methanamine (N4Py^{Me2}) ligand (Scheme 1). The identity of the complex in acetonitrile solution has been established using variable-temperature (VT) NMR, magnetic, and Mössbauer studies. The generation of an iron(IV)-oxo complex from **1** in acetonitrile and its reactivity toward external substrates along with the selectivity for aliphatic C–H bond cleavage and oxygen-atom-transfer reactions are presented in this work.

RESULTS AND DISCUSSION

Synthesis and Characterization. The pentadentate ligand N4Py^{Me2} was prepared by a reductive amination reaction between bis(6-methylpyridin-2-yl)methanamine⁶⁸ and pyridine-2-carboxaldehyde in dichloromethane. The iron(II) complex $[\text{Fe}^{\text{II}}(\text{N4Py}^{\text{Me2}})(\text{OTf})](\text{OTf})$ (**1**) was isolated as a light yellow solid from the reaction of equimolar amounts of $\text{Fe}(\text{OTf})_2 \cdot 2\text{MeCN}$ and ligand in dichloromethane, followed by washing the crude product with a mixture of dichloromethane and diethyl ether (Scheme 1 and Experimental Section).

The ESI-mass spectrum (positive ion mode in acetonitrile) of complex **1** exhibits an ion peak at m/z 225.6 with the isotope distribution pattern calculated for $[\text{Fe}(\text{N4Py}^{\text{Me2}})]^{2+}$ (Figure S1, Supporting Information). In the optical spectrum in acetonitrile, the complex displays charge-transfer bands at 455 nm (sh), 430 nm (sh), and 360 nm ($\epsilon \sim 1200 \text{ M}^{-1} \text{ cm}^{-1}$). These bands may be attributed to metal-to-ligand charge-transfer (MLCT) transitions (Figure S2, Supporting Information). The intensity of the charge-transfer bands is however weaker compared to other reported iron(II) complexes of N4Py-type ligands, indicating that the complex is high-spin.^{66,69}

Magnetic susceptibility measurements for a solid sample of **1** display a $\chi_{\text{M}}T$ value of $3.6 \text{ cm}^3 \text{ K mol}^{-1}$ in the region between 80 and 295 K, as expected for a high-spin iron(II) complex

(Figure S3, Supporting Information). With decreasing temperature below 80 K, the $\chi_M T$ value slowly decreases to $1.94 \text{ cm}^3 \text{ K mol}^{-1}$, likely due to the presence of zero field splitting ($|D| = 8.3 \text{ cm}^{-1}$). The ^{57}Fe Mössbauer spectrum of a solid sample of **1** measured in zero-field at 80 K with an isomer shift $\delta = 1.20 \text{ mm/s}$ and quadrupole splitting $\Delta E_Q = 3.18 \text{ mm/s}$ confirms the high-spin nature of the complex (Figure 1). Decreasing the temperature to 10 K does not change the spectral pattern of the solid sample (Figure S4, Supporting Information).

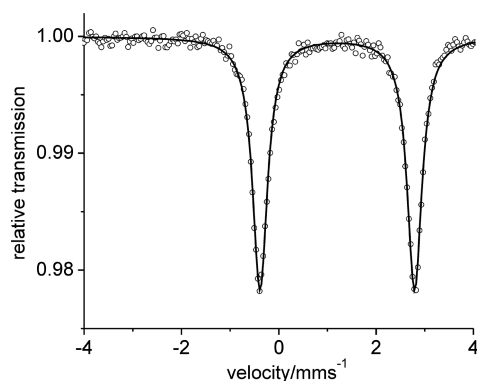


Figure 1. Zero-field ^{57}Fe Mössbauer spectrum of a solid sample of **1** measured at 80 K.

Having understood the spin state of **1** in the solid state, the spin state in solution was evaluated by VT ^1H NMR, Mössbauer, and magnetic measurements. In CD_3CN at 298 K, the ^1H NMR spectrum exhibits paramagnetically shifted proton resonances in the region from -30 ppm to 70 ppm (Figure S5, Supporting Information), typical of a high-spin nature of the complex. No appreciable change in the spectral pattern is observed except slight shifting of some signals upon decreasing the temperature to 233 K (Figure S5, Supporting Information). Thus, the complex remains high-spin within the accessible low-temperature limit for NMR measurements in CD_3CN . Interestingly, when Mössbauer measurements are carried out on a frozen sample of the complex in acetonitrile in zero field at 80 K, two species with nearly 1:1 ratio are observed: a high-spin species (54%) with $\delta = 1.16 \text{ mm/s}$ and $\Delta E_Q = 2.79 \text{ mm/s}$ and a low-spin species (46%) with $\delta = 0.51 \text{ mm/s}$ and $\Delta E_Q = 0.39 \text{ mm/s}$ (Figure 2). Upon increasing the temperature to 200 K, the proportion of the high-spin species increases to 82%, indicating the presence of spin-crossover (SCO) behavior in frozen solution. At 10 K, the high- and low-spin species remain in identical ratio as at 80 K (Figure S6, Supporting Information).

Since the Mössbauer measurements cover only the frozen solution temperature range, while NMR spectroscopy is restricted to the liquid solution phase, magnetic susceptibility measurements with a SQUID magnetometer were carried out on an acetonitrile solution of **1** to cover the entire temperature range between 295 and 2 K. The magnetic data are in accordance with both NMR and Mössbauer spectral data and provide a complete picture. The complex in acetonitrile is purely high-spin above ca. 220 K, but upon lowering the temperature, a gradual and incomplete SCO occurs until the ratio of high- and low-spin species becomes almost 1:1 at around 80 K (Figure 3). A further decrease of $\chi_M T$ is attributed to the zero-field splitting effect of the remaining high-spin species (cf. Figure S3, Supporting Information).

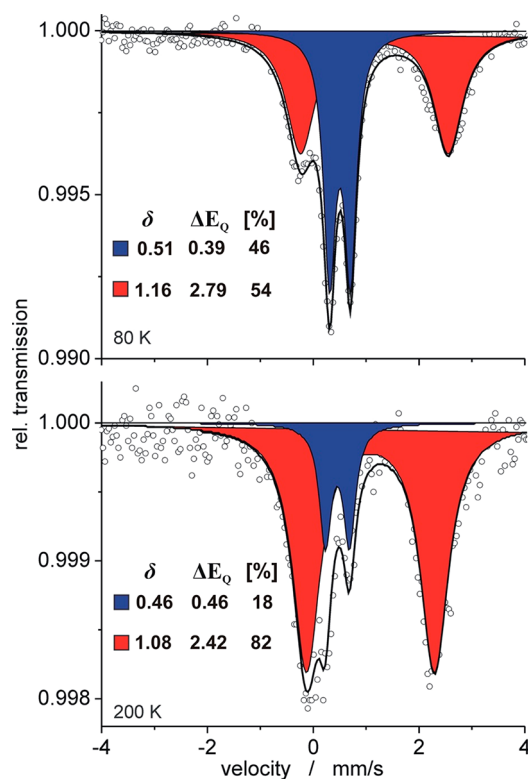


Figure 2. Zero-field ^{57}Fe Mössbauer spectrum of a frozen sample of **1** in acetonitrile measured at 80 K (top) and 200 K (bottom).

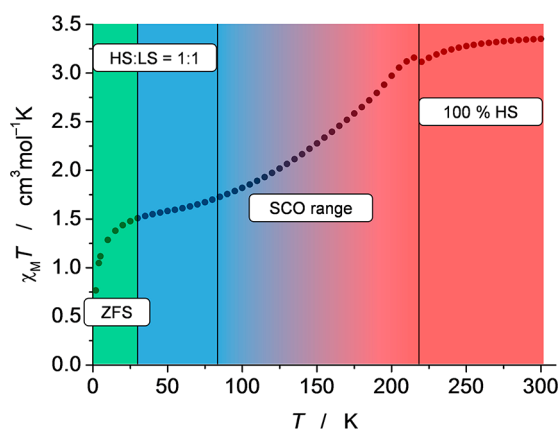


Figure 3. Variable-temperature magnetic data of **1** in acetonitrile (ZFS = zero-field splitting; SCO = spin crossover).

All the results discussed above support the idea that the species in acetonitrile can exhibit temperature-dependent SCO behavior, whereas the solid sample of **1** is purely high-spin. To evaluate the nature of the species generated in acetonitrile, ^{19}F NMR spectra of the sample were measured in two different solvents. The triflate anion, being a labile ligand, may easily be replaced by solvent molecules, leading to the formation of different species. In a coordinating solvent such as CH_3CN , the ^{19}F NMR spectrum of the complex displays a sharp resonance at -78 ppm (typical for free triflate anion), while a relatively broad signal at -50 ppm is observed in CD_2Cl_2 (Figures S7 and S8, Supporting Information, respectively). These results indicate that in acetonitrile, the triflate is noncoordinating,⁷⁰ while a fast exchange between coordinated and free triflate anion takes place in dichloromethane. It is thus assumed that

the triflate-coordinated high-spin species $[\text{Fe}^{\text{II}}(\text{N4Py}^{\text{Me2}})(\text{OTf})](\text{OTf})$ is present in CH_2Cl_2 solution and also in solid material of **1** that has been thoroughly washed with CH_2Cl_2 (in agreement with elemental analysis data). In contrast, complex **1** in acetonitrile converts to $[\text{Fe}^{\text{II}}(\text{N4Py}^{\text{Me2}})(\text{CH}_3\text{CN})](\text{OTf})_2$ (**1a**) as the dominant species. It remains unclear, however, why the SCO of **1a** is incomplete and reaches only a 1:1 ratio of high-spin and low-spin species at low temperatures; no evidence for dimerization of **1a** has been observed.

For structural characterization of the complex in the solid state, efforts were made to grow single crystals of **1**. Unfortunately, all attempts to isolate single crystals of **1** or **1a** with triflate counterion(s) were unsuccessful. However, X-ray quality single crystals of the perchlorate salt of **1a**, $[\text{Fe}(\text{N4Py}^{\text{Me2}})(\text{CH}_3\text{CN})](\text{ClO}_4)_2$ (**1b**), were grown by recrystallization of the complex (isolated from the reaction of iron(II) perchlorate hydrate and N4Py^{Me2} in acetonitrile) from a solvent mixture of acetonitrile and diethyl ether. A molecular view of the cationic part of complex **1b** is shown in Figure 4.

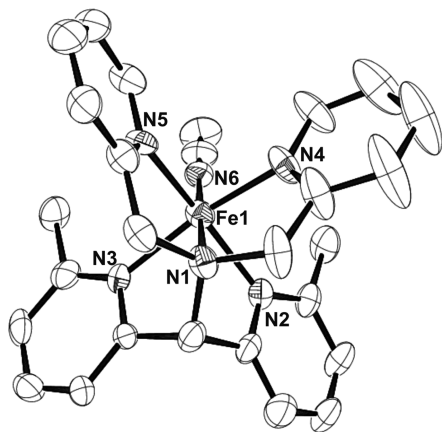


Figure 4. ORTEP plot of the complex cation of $[\text{Fe}^{\text{II}}(\text{N4Py}^{\text{Me2}})(\text{CH}_3\text{CN})]^{2+}$ (**1b**) with 30% thermal ellipsoids. All hydrogen atoms have been omitted for clarity.

The coordination environment around the iron center is distorted octahedral where the central iron is surrounded by five nitrogen donors from the ligand and the sixth coordination site is occupied by an acetonitrile molecule. The axial positions are occupied by the amine nitrogen (N1) and the nitrogen atom (N6) of the solvent molecule with the N1–Fe1–N6 angle being $178.6(4)^\circ$ (Table 1). The four pyridine nitrogen donors (N2, N3, N4, and N5) from the pentadentate ligand make the equatorial plane. The Fe–N bond distances vary in the range of 2.04–1.88 Å, and are in good agreement with the reported low-spin iron(II) complexes supported by N4Py-type ligands (Table 1).^{63,69,71} The Fe–N_{py} bonds for the pyridine moieties bearing 6-methyl groups are lengthened in the equatorial plane. There are thus two distinct sets of Fe–N_{py} distances; the two Fe–N_{py-6-Me} distances average approximately 2.04 Å, while the two Fe–N_{py} distances average approximately 1.98 Å. The elongation of the Fe–N_{py-6-Me} distances in **1b** relative to the analogous distances in the parent N4Py complex is ca. 0.07 Å (cf. Table 1). Similar elongated Fe–N_{py-6-Me} distances (average ca. 2.08 Å) have been observed in the related iron(II)-acetonitrile complex of the N4Py-type ligand, bis(pyridin-2-yl)-*N,N*-bis((6-methylpyridin-2-yl)methyl)methanamine ($[(\text{N2Py})(\text{N2CH}_2\text{Py}^{\text{Me}})]$).⁷² The steric hindrance of the 6-Me substituents prevents

Table 1. Comparison of Crystallographic Bond Distances (Å) and Angles (deg) of $[\text{Fe}^{\text{II}}(\text{N4Py}^{\text{Me2}})(\text{CH}_3\text{CN})]^{2+}$ (**1b**) and $[\text{Fe}^{\text{II}}(\text{N4Py})(\text{CH}_3\text{CN})]^{2+}$

bond distances and angles	$[\text{Fe}^{\text{II}}(\text{N4Py}^{\text{Me2}})(\text{CH}_3\text{CN})]^{2+}$ (1b)	$[\text{Fe}^{\text{II}}(\text{N4Py})(\text{CH}_3\text{CN})]^{2+}$ ^a
Fe1–N1	1.977(8)	1.961(3)
Fe1–N2	2.045(8)	1.976(3)
Fe1–N3	2.043(8)	1.967(3)
Fe1–N4	1.982(9)	1.968(3)
Fe1–N5	1.977(8)	1.975(3)
Fe1–N6	1.889(10)	1.915(3)
N1–Fe1–N2	81.6(4)	82.58(12)
N1–Fe1–N3	81.8(3)	82.56(11)
N1–Fe1–N4	83.2(4)	85.37(12)
N1–Fe1–N5	84.6(4)	85.29(12)
N1–Fe1–N6	178.6(4)	177.32(11)
N2–Fe1–N3	87.2(3)	87.12(11)
N2–Fe1–N4	88.5(4)	90.20(11)
N2–Fe1–N5	166.0(4)	167.71(13)
N2–Fe1–N6	97.1(4)	94.95(12)
N3–Fe1–N4	164.8(4)	167.87(13)
N3–Fe1–N5	92.9(3)	89.37(11)
N3–Fe1–N6	98.6(4)	96.32(12)
N4–Fe1–N5	87.8(4)	90.78(11)
N4–Fe1–N6	96.4(4)	95.69(12)
N5–Fe1–N6	96.7(4)	97.15(12)

^aRef 71.

adequate coordination of the 6-Me-pyridyl moieties to the metal and thus leads to lengthened bonds.

All the data for complex **1** discussed above are consistent with the introduction of the two methyl groups on the pyridine rings of the N4Py ligand weakening the ligand field, resulting in the formation of a high-spin iron(II)-triflate complex (**1**). Similar observations have been made for iron(II) complexes of weak field *N*-methylbenzimidazolyl/quinolyl-substituted N4Py ligands.^{66,67} Of note, the iron(II)-acetonitrile complex of the parent N4Py ligand remains low-spin in both solid state and in solution (Figure S9, Supporting Information). In contrast, the iron(II)-acetonitrile complex (**1a**) with a small energy gap between the high-spin and low-spin states exhibits temperature-dependent SCO behavior. This observation is consistent with that reported for substituted TPA ligands (TPA = tris(2-pyridylmethyl)amine), where methyl substitution on one of the pyridine rings of TPA is sufficient to cause a change in spin state from low-spin in $[\text{Fe}^{\text{II}}(\text{TPA})(\text{CH}_3\text{CN})_2]^{2+}$ to high-spin in $[\text{Fe}^{\text{II}}(6\text{-MeTPA})(\text{CH}_3\text{CN})_2]^{2+}$.⁷³

Generation and Characterization of an Iron(IV)-Oxo Complex. Complex **1**, upon treatment with a slight excess of *m*-CPBA in acetonitrile at -10°C , produces a pale green intermediate $[\text{Fe}^{\text{IV}}(\text{O})(\text{N4Py}^{\text{Me2}})]^{2+}$ (**2**) with an absorption band at $\lambda_{\text{max}} = 740\text{ nm}$ ($\epsilon \sim 220\text{ M}^{-1}\text{ cm}^{-1}$) (Figure 5). A titration experiment with **1** and *m*-CPBA in acetonitrile at -40°C suggests that 5 equiv of *m*-CPBA is required for maximum formation of **2** (Figure S10, Supporting Information). Thus, lowering the temperature does not change the yield of **2**. The formation of **2** is also observed at 25°C using oxone (2 equiv) as an oxidant. Complex **2** may also be generated in water upon reaction with ceric ammonium nitrate at 25°C ; however, a colloidal suspension is formed immediately after generation of **2**, making further investigations difficult. Moreover, the iron(IV)-oxo complex can be prepared from **1** using excess

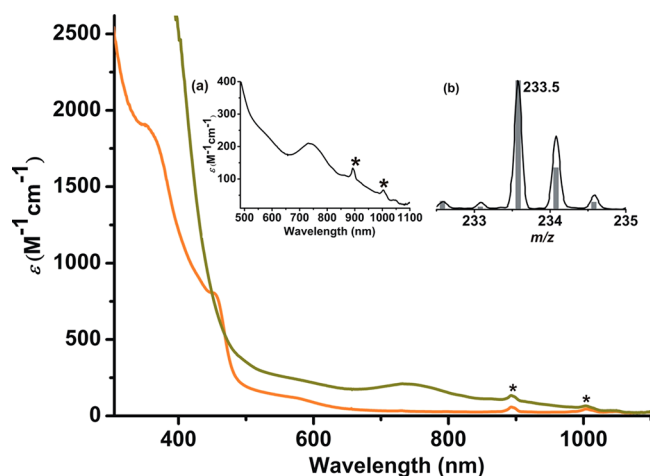


Figure 5. Optical spectrum of complex **2** (green line) generated upon treatment of **1** (orange line, 1 mM) with *m*-CPBA (5 equiv in acetonitrile) at $-10\text{ }^{\circ}\text{C}$. Inset: (a) Spectrum showing the region 500–1100 nm. (b) ESI-MS spectrum (positive ion mode in acetonitrile) of **2**. Spikes marked with * in the near-IR region likely arise from artifacts in the data collection process.

(20 equiv) solid PhIO at $-40\text{ }^{\circ}\text{C}$ but with low conversion. Since the precursor iron(II) complex (**1**) in acetonitrile remains purely high-spin in the temperature range mentioned above (Figure 3), the $S = 2$ iron(II) species leads to the formation of the iron(IV)-oxo species. In analogy with the optical spectra for reported iron(IV)-oxo complexes, the absorption band in the near IR region may be attributed to ligand field (d–d) transitions of the iron(IV) ion.⁷⁴ The ESI-mass spectrum (positive ion mode) of the green species displays ion peaks at m/z 233.5 with the isotope distribution patterns calculated for $[\text{Fe}(\text{O})(\text{N4Py}^{\text{Me2}})]^{2+}$ ($\text{C}_{25}\text{H}_{25}\text{FeN}_5\text{O}$ expected at m/z 233.5) (Figure 5, inset and Figure S11, inset a, Supporting Information). The half-life ($t_{1/2}$) of the intermediate species at $25\text{ }^{\circ}\text{C}$ is found to be 14 min (Figure S12, Supporting Information), demonstrating thermal instability of the species compared to the previously reported $S = 1$ iron(IV)-oxo complexes bearing mixed amine/pyridine donor pentadentate ligands (Table 2).^{33–35,42,66,75} Of note, the $[\text{Fe}(\text{O})(\text{N4Py})]^{2+}$ complex generated in acetonitrile with *m*-CPBA shows a half-life ($t_{1/2}$) value of 2 h at $25\text{ }^{\circ}\text{C}$ (Table 2), which is much shorter than the reported value of 60 h for the species generated with PhIO.³³ The shift of the near IR absorption band to lower energy compared to the iron(IV)-

oxo complex of the parent N4Py ligand ($\lambda_{\text{max}} = 695\text{ nm}$) further supports that the N4Py^{Me2} ligand engenders a weak ligand field in the equatorial plane in **2**.

The oxidation state and spin state of the iron center of **2** were evaluated by zero-field ^{57}Fe Mössbauer spectroscopy using a partially (20%) ^{57}Fe -enriched sample in frozen acetonitrile solution at 80 K. The main species (green subspectrum, 60%) in the spectrum (Figure 6) exhibits the

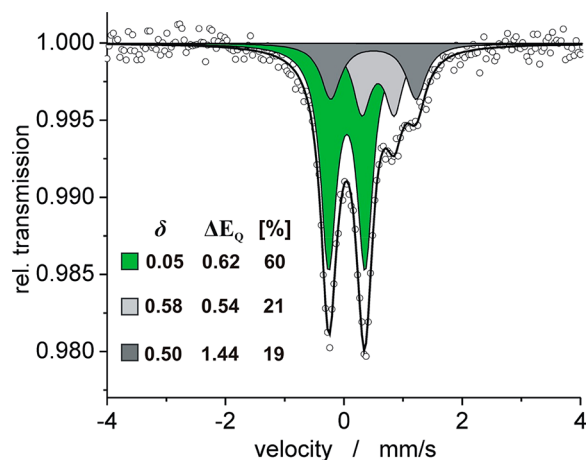


Figure 6. Zero-field ^{57}Fe Mössbauer spectrum of a frozen acetonitrile solution of **2** measured at 80 K.

Mössbauer parameters $\delta = 0.05\text{ mm/s}$ and $\Delta E_Q = 0.62\text{ mm/s}$, which are typical for N-ligated $S = 1$ iron(IV)-oxo complexes.²⁵ Thus, the pale green intermediate is an $S = 1$ iron(IV)-oxo species $[\text{Fe}^{\text{IV}}(\text{O})(\text{N4Py}^{\text{Me2}})]^{2+}$ (**2**). The remaining 40% species indicate the presence of decomposition products. In analogy with the Mössbauer parameters of an oxo-bridged diiron(III) species generated from the $[\text{Fe}^{\text{IV}}(\text{O})(\text{Bu-P2DA})]$ complex ($\delta = 0.46\text{ mm/s}$ and $\Delta E_Q = 1.65\text{ mm/s}$),⁷⁶ one of the iron(III) byproducts ($\delta = 0.50\text{ mm/s}$ and $\Delta E_Q = 1.44\text{ mm/s}$) is tentatively assigned to $[(\text{N4Py}^{\text{Me2}})\text{Fe}-\text{O}-\text{Fe}((\text{N4Py}^{\text{Me2}}))]^{4+}$, while the second one should be a mononuclear high-spin ferric species. No direct experimental evidence of a possible exchange of the oxygen atom of the iron(IV)-oxo species (**2**) with water was obtained.⁷⁷ Treatment of an acetonitrile solution of **2** with H_2^{18}O (98% ^{18}O enriched) did not result in the formation of any ^{18}O -incorporated species, as detected by mass spectrometry. Instead, the ESI-MS displays an ion peak at m/z 234.0 indicating partial decay of the iron(IV)-oxo to the

Table 2. Optical Spectral Properties and Stability of Different Fe(IV)-Oxo Complexes Supported by Different Pentadentate Ligands

complex	λ_{max} nm (ϵ , $\text{M}^{-1}\text{ s}^{-1}$)	$t_{1/2}$ at 298 K	refs
$[\text{Fe}^{\text{IV}}(\text{O})(\text{N4Py}^{\text{Me2}})]^{2+}$	740 (220)	14 min	this work
$[\text{Fe}^{\text{IV}}(\text{O})(\text{N4Py})]^{2+}$	695 (400)	60 h ^a	33
$[\text{Fe}^{\text{IV}}(\text{O})(\text{Bn-tpen})]^{2+}$	739 (400)	6 h	33
$[\text{Fe}^{\text{IV}}(\text{O})(\text{TMC-Py})]^{2+}$	834 (260)	7 h	42
$[\text{Fe}^{\text{IV}}(\text{O})(\text{Py}_2\text{TACN})]^{2+}$	740(340) 900 (200)	not reported	35
$[\text{Fe}^{\text{IV}}(\text{O})(\text{BisPi1})]^{2+}$	728(400)	not reported	75, 99
$[\text{Fe}^{\text{IV}}(\text{O})(\text{BisPi2})]^{2+}$	728(380)	not reported	75
$[\text{Fe}^{\text{IV}}(\text{O})(\text{N}_3\text{Py}-(\text{NMB}))]^{2+}$	708 (400)	40 h	66
$[\text{Fe}^{\text{IV}}(\text{O})(\text{N}_2\text{Py}-(\text{NMB})_2)]^{2+}$	725 (380)	2.5 h	66
$[\text{Fe}^{\text{IV}}(\text{O})(\text{N}_2\text{Py}2\text{Q})]^{2+}$	770 (380)	2.5 h	67

^aThe iron(IV)-oxo complex generated from the precursor iron(II) complex with *m*-CPBA in acetonitrile exhibits a $t_{1/2}$ value of 2 h at 298 K.

corresponding iron(III)-hydroxide species, $[\text{Fe}(\text{OH})\text{-(N4Py}^{\text{Me2}})]^{2+}$ (Figure S11, inset b, Supporting Information). However, no intraligand hydroxylated product was observed in the self-decay pathway. The thermal instability of **2** does not permit the observation of any intermediate to a full extent due to the partial decay of the complex in the process of transferring the sample for Mössbauer measurements.

Reactivity of the Iron(IV)-Oxo Complex (2). The observed short lifetime of **2** indicates that the complex would exhibit enhanced reactivity toward external substrates in comparison to the parent N4Py complex. The oxygen-atom-transfer (OAT) ability of **2** was tested using methyl phenyl sulfide (PhSMe) as a substrate at $-10\text{ }^\circ\text{C}$. The fast decay of the band at 740 nm compared to the self-decay rate of **2** suggests oxidation of phenyl methyl sulfide. During the course of the reaction, **2** was converted into its iron(II) precursor complex **1** with a clear isosbestic point at 660 nm (Figure 7).

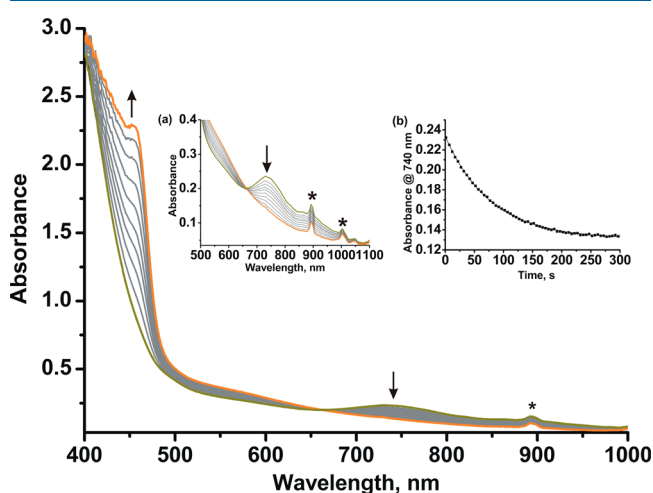


Figure 7. Decay of **2** in the presence of thioanisole (5 equiv) with concomitant formation of **1** at $-10\text{ }^\circ\text{C}$ in acetonitrile. Inset: (a) Spectrum in the region between 500 and 1100 nm. (b) Time course of the decay monitored at 740 nm. Spikes marked with * likely arise from artifacts in the data collection process.

The reaction follows a pseudo-first-order behavior in the presence of excess substrate (5–20 equiv). The observed rate constant was found to depend linearly on the substrate concentration enabling extraction of the second-order rate constant (k_2). The k_2 value of $1.03 (\pm 0.03)$ is at least 3–100-fold higher than the values obtained for most of the reported

iron-oxo species supported by mixed amine/pyridine donor pentadentate ligands.³⁵ A comparison of oxo-atom-transfer reaction rates of **2** and other reported synthetic $S = 1$ iron(IV)-oxo complexes supported by mixed amine/pyridine donor ligands is shown in Table 3.

A series of alkane substrates having C–H BDEs ranging from 77 to 99.3 kcal/mol were used to test the reactivity of **2** toward hydrogen atom abstraction. Under pseudo-first-order reaction conditions, the band at 740 nm decays rapidly in the presence of 9,10-dihydroanthracene (5 equiv) at $-10\text{ }^\circ\text{C}$ (Figure S13, Supporting Information). The linear dependence of rate on substrate concentration yields the second-order rate constant values of $1.7 \times 10^{-1}\text{ M}^{-1}\text{ s}^{-1}$ and $2.0\text{ M}^{-1}\text{ s}^{-1}$ at -10 and $25\text{ }^\circ\text{C}$, respectively (Figure S14e, Supporting Information and Table 3).

Other substrates such as 1,4-cyclohexadiene (1,4-CHD), ethylbenzene (PhEt), toluene (PhCH_3), 2,3-dimethylbutane (2,3-DMB), and cyclohexane (*cyclo*- C_6H_{12}) were also used to test the reactivity of **2** toward hydrogen atom abstraction. Second-order rate constants (k_2) at 298 K for these substrates were determined (Table 4, and Figure S14, Supporting

Table 4. Comparison of Second-Order Rate Constant for the Reaction of $[\text{Fe}^{\text{IV}}(\text{O})(\text{N4Py}^{\text{Me2}})]^{2+}$ and $[\text{Fe}^{\text{IV}}(\text{O})(\text{N4Py})]^{2+}$ with Various Alkane Substrates at 298 K

substrate (BDE in kcal/mol)	$[\text{Fe}^{\text{IV}}(\text{O})(\text{N4Py}^{\text{Me2}})]^{2+}$ k_2 ($\text{M}^{-1}\text{ s}^{-1}$)	$[\text{Fe}^{\text{IV}}(\text{O})(\text{N4Py})]^{2+}$ k_2 ($\text{M}^{-1}\text{ s}^{-1}$) ^a	$[\text{Fe}^{\text{IV}}(\text{O})(\text{N4Py})]^{2+}$ k_2 ($\text{M}^{-1}\text{ s}^{-1}$) ^b
9,10-DHA (77)	2.0	18.0	13.1
1,4-CHD (78)	0.79	10.69	10.4
PhEt (87)	7.62×10^{-3}	4.0×10^{-3}	3.0×10^{-3}
PhCH_3 (90)	3.54×10^{-3}	6.3×10^{-4}	8.3×10^{-4}
2,3-DMB (96.5)	1.78×10^{-3}	1.2×10^{-4}	1.6×10^{-4}
<i>cyclo</i> - C_6H_{12} (99.3)	6.73×10^{-4}	5.5×10^{-5}	6.7×10^{-5}

^aData taken from refs 31, 33, and 35 except that for 1,4-CHD. ^bValues obtained with the iron(IV)-oxo species generated with *m*-CPBA in acetonitrile.

Information) which afforded the corrected k_2' based on the number of abstractable weak C–H bonds for each substrate. The iron-oxo species **2** is efficient in C–H bond cleavage of aliphatic substrates and shows a reasonable linear correlation between $\log k_2'$ and the C–H BDE of the substrates (Figure 8). This linear correlation indicates that the reactions of **2** with the substrates take place via the rate-determining transfer of a hydrogen atom, as established earlier for other related iron(IV)-oxo complexes.^{32,33,78} From the plot in Figure 8, it

Table 3. Oxygen-Atom-Transfer and Hydrogen Atom Abstraction Reactivity of Different Fe(IV)-Oxo Complexes Supported by Different Pentadentate Ligands

substrate, complex	thioanisole (263 K) k_2 ($\text{M}^{-1}\text{ s}^{-1}$)	cyclohexane (298 K) k_2 ($\text{M}^{-1}\text{ s}^{-1}$)	9,10-DHA k_2 ($\text{M}^{-1}\text{ s}^{-1}$)	ref
$[\text{Fe}^{\text{IV}}(\text{O})(\text{N4Py}^{\text{Me2}})]^{2+}$ (2)	1.03 (± 0.03)	6.73×10^{-4}	2 (± 0.07) at 298 K [0.17 (± 0.01) at 263 K]	this work
$[\text{Fe}^{\text{IV}}(\text{O})(\text{N4Py})]^{2+}$	0.014	6.7×10^{-5} ^a	13.10 at 298 K ^a	31, 35
$[\text{Fe}^{\text{IV}}(\text{O})(\text{Bn-tpen})]^{2+}$	0.33	3.9×10^{-4}	100 at 298 K	35
$[\text{Fe}^{\text{IV}}(\text{O})(\text{Py}_2\text{TACN})]^{2+}$	0.004	not reported	7.4 at 298 K	35
$[\text{Fe}^{\text{IV}}(\text{O})(\text{BisPi1})]^{2+}$	0.024	not reported	1.1 at 298 K	35
$[\text{Fe}^{\text{IV}}(\text{O})(\text{BisPi2})]^{2+}$	2.4	not reported	40 at 298 K	35
$[\text{Fe}^{\text{IV}}(\text{O})(\text{N}_3\text{Py-(NMB)})]^{2+}$	0.033 (at 243 K)	3.0×10^{-4}	not reported	66
$[\text{Fe}^{\text{IV}}(\text{O})(\text{N}_2\text{Py-(NMB)})_2]^{2+}$	0.31 (at 243 K)	2.9×10^{-3}	1.4 (at 243 K)	66
$[\text{Fe}^{\text{IV}}(\text{O})(\text{N}_2\text{Py2Q})]^{2+}$	7.4 (at 233 K)	2.9×10^{-2}	not reported	67

^aValues obtained with the iron(IV)-oxo species generated with *m*-CPBA in acetonitrile.

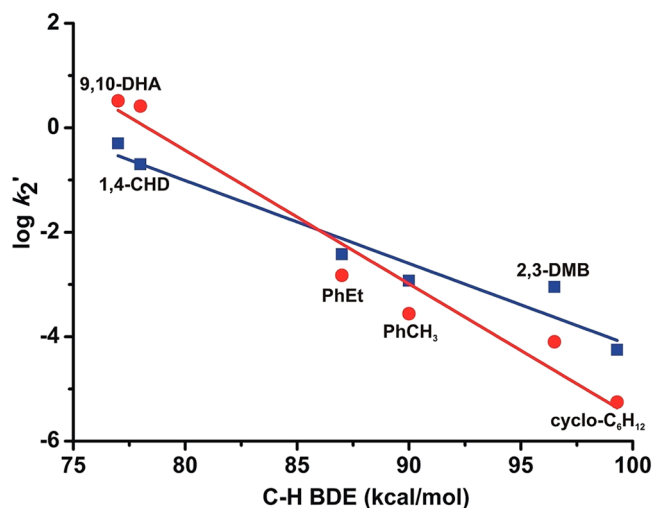


Figure 8. Plot of $\log k_2'$ versus C–H BDEs of different substrates in the oxidation by $[\text{Fe}^{\text{IV}}(\text{O})(\text{N4Py}^{\text{Me2}})]^{2+}$ (blue squares) and $[\text{Fe}^{\text{IV}}(\text{O})(\text{N4Py})]^{2+}$ (red circles). k_2' is obtained by dividing the second-order rate constant by the number of abstractable C–H bonds on the substrate.

is clear that the differences in hydrogen-atom-transfer (HAT) rate between **2** and the $[\text{Fe}^{\text{IV}}(\text{O})(\text{N4Py})]^{2+}$ complex diminish as the substrate C–H bonds become weaker, resulting in a smaller slope for **2**. Notably, the two lines cross at around 86 kcal/mol, and the hydrogen atom affinity of the iron(IV)-oxo unit of **2** is lower with decreasing C–H BDE. The almost similar values of the second-order rate constants obtained with 9,10-DHA and 1,4-CHD substrates indicate that the steric factor of 6-Me substitution does not play a major role in the HAT reactivity of **2**.

The second-order rate constants for separate reactions between intermediate **2** and toluene and toluene- d_8 yielded a primary kinetic isotope effect value of 14 (Figure S15,

Supporting Information). The observed KIE value is lower than that reported for $[\text{Fe}^{\text{IV}}(\text{O})(\text{N4Py})]^{2+}$,⁷⁹ but similar to those for the iron(IV)-oxo complexes of N4Py-derived ligands.⁶⁶ Thus, the nonclassical KIE value is indicative of a reaction pathway that is very similar to that proposed for HAT reactions by iron(IV)-oxo complexes.

It has been demonstrated that weakening the ligand field of the iron(IV)-oxo complex by replacing one of the four nitrogen donors of the tetramethylcyclam (TMC) or 1,4,7,11-tetramethyl-1,4,7,11-tetraazacyclotetradecane (TMCN) ligands by an oxygen donor dramatically increases the OAT and HAT reactivity.⁸⁰ Similar observations have been made with iron(IV)-oxo complexes based on N4Py-type ligands with *N*-methylbenzimidazole or quinoline donors.^{66,67} The weakening of the ligand field in **2** increases the electrophilicity of the iron-oxo unit resulting in faster HAT reactivity, especially in case of less acidic C–H groups. When compared with iron(IV)-oxo complexes with other N5 ligands bearing mixed amine and pyridine donors, the rates of HAT by **2** with aliphatic substrates having C–H BDE > 86 kcal/mol are faster than the $[\text{Fe}^{\text{IV}}(\text{O})(\text{N4Py})]^{2+}$ complex, whereas the reactivity of **2** in cyclohexane oxidation is almost comparable to that of $[\text{Fe}^{\text{IV}}(\text{O})(\text{BnTPEN})]^{2+}$ (Table 3). However, **2** is less reactive than the $[\text{Fe}^{\text{IV}}(\text{O})(\text{N2Py2Q})]^{2+}$ complex (N2Py2Q = 1,1-di(pyridin-2-yl)-*N,N*-bis(quinolin-2-ylmethyl)-methanamine).⁶⁷ The latter is almost 75-fold more reactive toward thioanisole and 40-fold more reactive in cyclohexane hydroxylation. Interestingly, complex **2** is 70-fold more reactive in thioanisole oxidation at -10 °C and 10-fold more reactive in hydroxylating cyclohexane at 25 °C than the parent $[\text{Fe}^{\text{IV}}(\text{O})(\text{N4Py})]^{2+}$ complex but is 7-fold slower in oxidizing 9,10-DHA. Given the short half-life (14 min) of **2**, this is a surprising trend that is difficult to rationalize. It may be argued that the slow HAT observed for oxidation of 9,10-DHA and 1,4-CHD may be due to restricted orientations in the approach of the substrates to **2** due to steric interactions, but this is

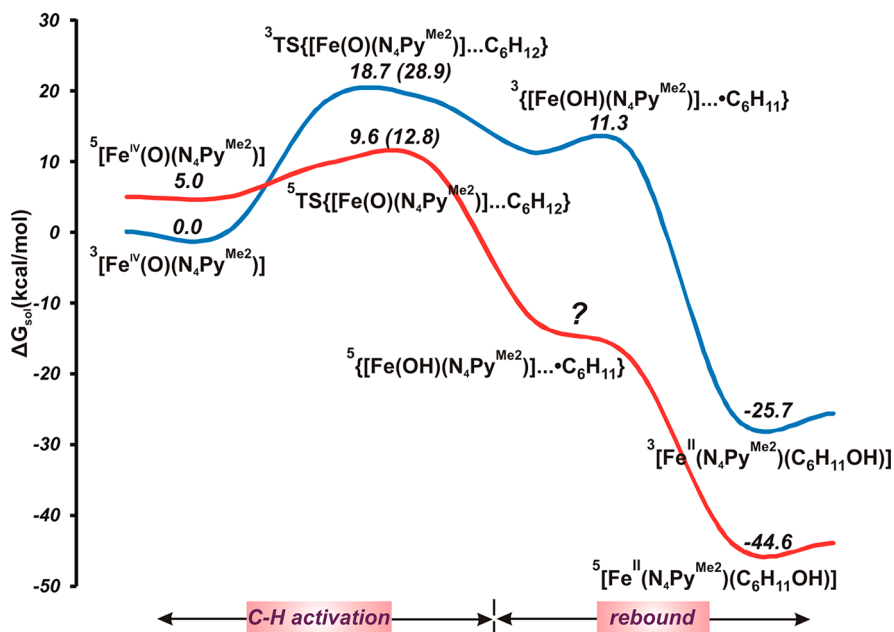


Figure 9. Relative condensed phase free energy profile for the reaction of **2** (triplet and quintet) with cyclohexane (C_6H_{12}) at the UB3LYP-D3(CPCM)/6-31++G(d,p)/Fe(SDD)//UB3LYP/6-31++G(d,p)/Fe(SDD) level of theory. The free energy values given in brackets for transition states indicate the values for the corresponding spin states of $[\text{Fe}^{\text{IV}}(\text{O})(\text{N4Py})]^{2+}$.

contradicted by the fact that the observed HAT rates for the two substrates are very similar (vide supra) and that the HAT rates for the iron(IV)–O complexes with the sterically hindered bis-quinoline and bis(methyl)benzimidazolyl derivatives of N4Py are more reactive across the board in reactions with the same substrates, relative to the parent N4Py complex (Table 3).^{66,67,81}

To understand the mechanism of the substrate oxidation by complex **2**, the reaction pathways were investigated by density functional theory (DFT) calculations (see Experimental Section for details). Oxygenation of C–H bonds by a high valent iron-oxo species has been reported to take place via two steps: The first step involves the HAT from the targeted C–H bond followed by an oxygen rebound in the second step. In almost all cases, the HAT step is rate determining, and the observed KIE (vide supra) indicates that this is the case also for **2**.^{61,62,82,83} HAT pathways for the reaction of **2** with cyclohexane were computed on the triplet and quintet surfaces and compared with those of the $[\text{Fe}^{\text{IV}}(\text{O})(\text{N4Py})]^{2+}$ complex (Figure 9). In both cases, the triplet state was found to be the ground state. The triplet–quintet energy gap was predicted to be 9.4 kcal/mol for $[\text{Fe}^{\text{IV}}(\text{O})(\text{N4Py})]^{2+}$, whereas for **2**, the gap reduces to 6.9 kcal/mol (Supporting Information). The corresponding condensed phase free energy gaps, $\Delta G_{\text{TQ}}(\text{sol})$, are 7.4 and 5.0 kcal/mol for $[\text{Fe}^{\text{IV}}(\text{O})(\text{N4Py})]^{2+}$ and **2**, respectively.

HAT from the $\sigma(\text{C–H})$ of an alkane to the LUMO of $[\text{Fe}^{\text{IV}}(\text{O})(\text{L})]$ species may take place either in the quintet or in triplet spin state. The singly occupied $\pi^*d_{xz/yz}$ and the unoccupied $\sigma^*d_z^2$ frontier orbitals of the triplet iron(IV)-oxo species are involved in the HAT step. Because of the presence of the $\pi^*d_{xz/yz}$ orbital, the π -attack requires a $\text{Fe}=\text{O}\cdots\text{HC}$ bond angle of $\sim 120^\circ$ (bent TS) for better overlap between the $\sigma(\text{C–H})$ and the $p_{x/y}$ of the oxygen atoms of the oxo unit. In the quintet spin state, the LUMO turned out to be the $\sigma^*d_z^2$ orbital. Therefore, the C–H σ -bond vertically approaches the $\text{Fe}=\text{O}$ unit with a $\text{Fe–O}\cdots\text{HC}$ angle of $\sim 180^\circ$ (linear TS) to ensure the best overlap between $\sigma(\text{C–H})$ and $\sigma^*d_z^2$ during σ -attack.

In the case of C–H activation by the iron(IV)-oxo complexes, the calculated transition state on the quintet surface is lower than that on the triplet surface, that is, a crossover of spin states in the transition state takes place (Figures 9 and 10 and Figure S16, Supporting Information). The low triplet–quintet gap (ΔE_{TQ}) makes the excited quintet state more accessible, resulting in a lower kinetic barrier for the C–H cleavage. For **2**, the barriers for HAT in the triplet and quintet states turned out to be 18.7 and 9.6 kcal/mol, respectively. For $[\text{Fe}^{\text{IV}}(\text{O})(\text{N4Py})]^{2+}$, those values are much higher at 28.9 and 12.8 kcal/mol, respectively (Figure 9). Thus, the lower barriers in case of **2** clearly support the faster reactivity of the complex compared to $[\text{Fe}^{\text{IV}}(\text{O})(\text{N4Py})]^{2+}$. After C–H bond activation, the O–C bond formation takes place via a rebound mechanism, which is a thermodynamically downhill process. Of note, a radical pair is not observed in the quintet surface. Following the HAT step, the rebound step takes place without any distinct barrier (Figure 9), which ultimately leads to a hydroxylated product. The computational modeling of cyclohexane oxidation is in agreement with the two-state reactivity (TSR) model.⁶¹

The activation barriers for 9,10-DHA are computed to be quite low compared to those of cyclohexane, which are consistent with the experimental observation. The approach of

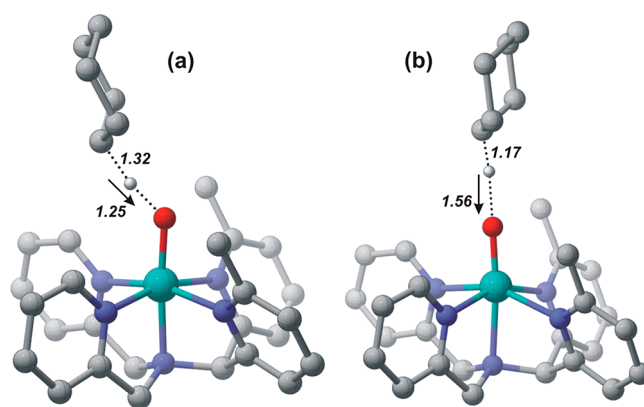


Figure 10. Energy optimized geometries of the transition states of C–H bond activation of cyclohexane by $[\text{Fe}^{\text{IV}}(\text{O})(\text{N4Py}^{\text{Me2}})]^{2+}$ in (a) triplet spin state and (b) in quintet spin state at the UB3LYP/6-31++G(d,p)/Fe(SDD) level of theory.

9,10-DHA takes place at the opposite side of the 6-Me groups of the ligand in **2**. As observed experimentally, the steric factor is less likely to play any role on the rate of HAT with 9,10-DHA. For both the iron(IV)-oxo complexes, $[\text{Fe}^{\text{IV}}(\text{O})(\text{N4Py}^{\text{Me2}})]^{2+}$ (**2**) and $[\text{Fe}^{\text{IV}}(\text{O})(\text{N4Py})]^{2+}$, the activation barriers for the quintet transition states are negative with respect to the quintet states of the corresponding iron-oxo complexes (Figure S17). However, the barriers for the triplet states are found at 8.4 and 7.2 kcal/mol for **2** and $[\text{Fe}^{\text{IV}}(\text{O})(\text{N4Py})]^{2+}$, respectively. In the TSR model, the kinetic barrier is predicted to be a weighted average of the barrier in the ground triplet and the corresponding excited quintet states.^{61,62,83} As the barriers for the TS on the quintet surface are negative, the rate-determining C–H bond activation rate may be primarily governed by the triplet state indicating slightly faster C–H activation by $[\text{Fe}^{\text{IV}}(\text{O})(\text{N4Py})]^{2+}$ as observed experimentally. However, this small energy gap cannot be reliably predicted considering the error limit of the DFT level of theory. Thus, further investigations to characterize the electronic structure of the iron(IV) complex (**2**) are warranted to unravel the unusual trend in HAT reactivity.

The relative strengths of iron-oxo bonds in the complexes $[\text{Fe}^{\text{IV}}(\text{O})(\text{N4Py})]^{2+}$ and $[\text{Fe}^{\text{IV}}(\text{O})(\text{N4Py}^{\text{Me2}})]^{2+}$ (**2**) were estimated from the $\text{Fe}=\text{O}$ stretching frequency. The infrared (IR) and Raman intensities associated with all normal modes for both the noncentrosymmetric molecules were computed at the B3LYP/6-31++G(d,p) level of theory. The computed symmetric (with respect to the $\text{Fe–N}_{\text{trans}}$ bond) $\text{Fe}=\text{O}$ stretching frequencies were identified by the marked Raman intensities over IR intensities and the $\text{Fe}=\text{O}$ stretching (with respect to the $\text{trans Fe–N}_{\text{trans}}$ bond) frequencies were observed at 938 and 919 cm^{-1} for $[\text{Fe}^{\text{IV}}(\text{O})(\text{N4Py})]^{2+}$ and $[\text{Fe}^{\text{IV}}(\text{O})(\text{N4Py}^{\text{Me2}})]^{2+}$, respectively (Table S1, Supporting Information). It is important to mention here that the DFT predicted $\text{Fe}=\text{O}$ stretching frequency is larger than the experimentally reported value (841 cm^{-1})⁸⁴ for the $[\text{Fe}^{\text{IV}}(\text{O})(\text{N4Py})]^{2+}$ complex. However, it has been reported that the B3LYP functional systematically overestimates $\text{Fe}=\text{O}$ stretching frequencies by $\sim 50 \text{ cm}^{-1}$,^{84,85} and therefore considering the intrinsic methodical error, the B3LYP-predicted frequency of 919 cm^{-1} closely scales to the experimentally reported value of nonheme iron(IV)-oxo complexes. Nevertheless, the presence of 6-methyl groups on the pyridine rings of N4Py^{Me2} ligand

weakens the iron-oxo bond relative to the parent N4Py complex, as reflected in the corresponding stretching frequencies.

The DFT-optimized structural data for **2** (Table S2, Supporting Information) were considered further to understand the difference in HAT and OAT reactivity of the iron(IV)-oxo complexes of N4Py-type ligands. It has recently been suggested that the higher reactivity of $[\text{Fe}^{\text{IV}}(\text{O})\text{-(N}_2\text{Py}_2\text{Q)}]^{2+}$ arises from the 10° tilt of the $\text{Fe}=\text{O}$ unit, observed in its crystal structure, away from the z -axis of the complex due to steric interactions with the quinoline donors.⁶⁷ On the other hand, the DFT calculated structure of **2** reveals that the $\text{Fe}=\text{O}$ unit is only tilted 3° from the z axis and in the opposite direction. It may be noted that no such tilt is observed in $[\text{Fe}^{\text{IV}}(\text{O})(\text{N}_4\text{Py})]^{2+}$ complex.³⁸ The tilt of the $\text{Fe}=\text{O}$ unit toward the more sterically hindering 6-Me-pyridyl donor moieties appears counterintuitive, but is almost negligible. A similar tilt of the acetonitrile ligand toward the 6-Me-Py moieties is also observed in the crystal structure of **1b** (vide supra). A close scrutiny of this structure shows that once the $\text{Fe}-\text{N}$ distances to the 6-Me-Py groups are elongated, the steric encumbrance by these moieties is no greater than that of the pyridyl moieties. As shown in Figure 11, the distances

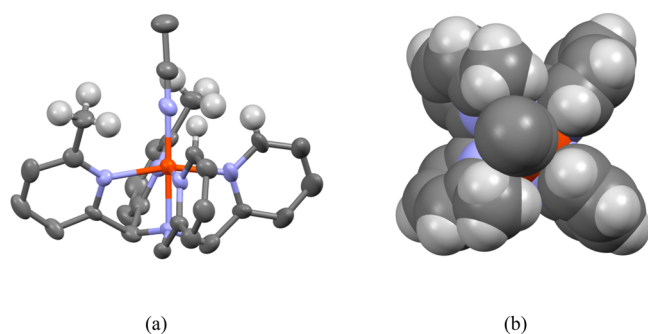


Figure 11. (a) A Mercury plot of the molecular structure of **1b**, showing the hydrogens of the 6-methyl substituents and the 6-H hydrogens of the nonsubstituted pyridyl groups. (b) A corresponding space-filling plot, viewed down the molecular z -axis; the hydrogen atoms of the acetonitrile ligand have been omitted for the sake of clarity.

between the 6-H hydrogens of the nonsubstituted pyridyl moieties and the nitrogen atom in the acetonitrile ligand are the same as the shortest distances between that nitrogen and the hydrogens of the 6-methyl substituents (2.67 Å) (Table S3, Supporting Information). The tilt of the acetonitrile ligand in complex **1b** and the corresponding computed tilt in **2** (vide supra) are thus not unreasonable.

Comparing the crystallographically determined structures of the iron(IV)-oxo complexes $[\text{Fe}^{\text{IV}}(\text{O})(\text{N}_4\text{Py})]^{2+}$,³⁸ $[\text{Fe}^{\text{IV}}(\text{O})\text{-(N}_2\text{Py-(NMB)}_2)]^{2+}$, and $[\text{Fe}^{\text{IV}}(\text{O})(\text{N}_2\text{Py}_2\text{Q})]^{2+}$ ($\text{N}_2\text{Py-(NMB)}_2 = N,N\text{-bis}((1\text{-methyl-1H-benzoimidazol-2-yl-methyl})-1,1\text{-di(pyridin-2-yl)methanamine})$) to those of the analogous iron(II)-acetonitrile complexes (Table 5),^{66,67,81} it may be noted that there is a direct correlation between the structural trends in the two types of complexes with respect to equatorial $\text{Fe}-\text{N}$ distances and tilt of axial ligand (both degree and direction of ligand tilt). Assuming that this correlation holds also for other N4Py-type ligands, it may be predicted that the iron(IV)-oxo complex of bis(pyridin-2-yl)- $N,N\text{-bis}((6\text{-methylpyridin-2-yl)methyl)methanamine}$, (N_2Py)-

Table 5. Comparison of the Bond Parameters in Iron(II) and Iron(IV) Complexes of N4Py-Type Ligands

complex	$\text{Fe}=\text{O}$	$\text{Fe}-\text{N}_{\text{amine}}$	$\text{Fe}-\text{N}_{\text{py}}$	$\text{Fe}-\text{N}_{\text{Q}}$	$\text{Fe}-\text{N}_{\text{NMB}}$	$\text{Fe}-\text{N}_{\text{CH}_3\text{Py}}$	$\text{Fe}-\text{N}_{\text{MeCN}}$	$\angle \text{N}_{\text{amine}}-\text{Fe}-\text{N}_{\text{X}}$	ref
$[\text{Fe}^{\text{IV}}(\text{O})(\text{N}_4\text{Py})]^{2+}$	1.639(5)	2.033(8)	1.964(5)	—	—	1.949(5)	—	179.4(3) (X = O)	38
$[\text{Fe}^{\text{II}}(\text{N}_4\text{Py})(\text{MeCN})]^{2+}$	—	1.961(3)	1.976(3) 1.967(3)	—	—	1.968(3) 1.975(3)	1.915(3)	177.32(11) (X = MeCN)	71
$[\text{Fe}^{\text{IV}}(\text{O})(\text{N}_2\text{Py}_2\text{Q})]^{2+}$	1.677(5)	2.084(4)	2.023(4) 2.022(4)	2.073(4) 2.067(4)	—	—	—	170.5(2) (X = O)	67, 81
$[\text{Fe}^{\text{II}}(\text{N}_2\text{Py}_2\text{Q})(\text{MeCN})]^{2+}$	—	2.020(4)	2.019(4) 2.012(5)	2.102(5) 2.092(4)	—	—	1.954(6)	166.79(19) (X = MeCN)	81
$[\text{Fe}^{\text{IV}}(\text{O})(\text{N}_2\text{Py-(NMB)}_2)]^{2+}$	1.656(4)	2.115(6)	1.995(5) 1.983(5)	—	1.950(5) 1.954(5)	—	—	177.0(2) (X = O)	66
$[\text{Fe}^{\text{II}}(\text{N}_2\text{Py-(NMB)}_2)(\text{MeCN})]^{2+}$	—	2.028(3)	1.964(3) 1.983(3)	—	1.983(3) 1.979(2)	—	1.901(3)	176.64(11) (X = MeCN)	66

(N2CH₂Py^{Me}),⁷² shall exhibit a reactivity on par with that of the most reactive of the Fe(IV)=O complexes, [Fe^{IV}(O)-(N2Py2Q)]²⁺, since the iron(II)-acetonitrile complexes of the two ligands exhibit very similar structural parameters (Table 6), including tilts of the axial ligands that exceed 10°. We are currently investigating this matter.

From the decay patterns of **2** in the presence of thioanisole and 9,10-DHA, it is clear that the iron(II) complex is regenerated after the reaction (Figure 7 and Figure S13, Supporting Information). This prompted us to investigate the reactivity of **1** for catalytic oxidations using oxone (KHSO₅) as the oxidant. For these catalytic reactions, use of *m*-CPBA was avoided in order to exclude that this strong oxidant would cause direct oxidation of substrates without the mediation of a metal-based oxidant. The catalytic abilities of **1** and [Fe^{II}(N4Py)(CH₃CN)]²⁺ were compared under similar reaction conditions using different substrates. With complex **1**, cyclohexane oxidation resulted in cyclohexanol and cyclohexanone with an overall yield of 25% (based on oxone) and with an alcohol to ketone ratio (A/K) of 2.7. It may be noted that poor yields of oxidation products (10%) and a low A/K ratio (0.5) were obtained for cyclohexane oxidation by [Fe^{II}(N4Py)(CH₃CN)]²⁺ under similar experimental conditions. In addition, **1** was found to oxidize adamantane with a C3/C2 normalized selectivity of 22. Such high C3/C2 selectivity (11–48) was observed for oxidations with PhIO catalyzed by P450 mimics.⁸⁶ Other substrates such as 9,10-DHA, fluorene, ethylbenzene, toluene, and 1,4-cyclohexadiene (1,4-CHD) were also oxidized by **1** using oxone as the oxidant (Table 7).

The observed reactivity for **2** and the computational results are in agreement with an oxygen rebound mechanism in C–H bond activation reactions. With cyclohexene, however, allylic oxidation products were obtained, and the efficiency with respect to consumption of oxidant was around 90%. The alcohol to ketone ratio (A/K) of 3.4 is greater than the A/K ratio of 1.7 obtained for the less selective [Fe^{II}(N4Py)-(CH₃CN)]²⁺ system. The observation of allylic oxidation products in cyclohexene oxidation suggests that this reaction may proceed via a non-rebound mechanism.^{87–89} Substrates such as 1-octene and styrene were converted to 1-octeneepoxide and benzaldehyde, respectively. Complex **1** also carries out the oxidation of benzyl alcohol and thioanisole to afford benzaldehyde and thioanisole oxide, respectively. The yields of the products from different substrates are listed in Table 7. For aliphatic substrates, some degree of catalytic activity supports that HAT reactions can reform the iron(II) precursor. While the catalytic activity of the complex is low, the selectivity for substrate oxidation is higher compared to other related complexes. The detection of oxo-bridged diiron(III) species or mononuclear iron(III) complex as decay products in the Mössbauer spectrum indicates their formation during decay of the iron(IV)-oxo complex (**2**). Therefore an active iron(IV)-oxo species in the catalytic reaction may form inactive dimeric species or may undergo degradation to some unproductive pathway, resulting in low catalytic turnover.

SUMMARY AND CONCLUSION

We have reported the isolation and characterization of an iron(II) complex supported by a substituted N4Py ligand. The ligand forms a high-spin iron(II)-triflate complex in the solid state. In acetonitrile solution, however, the triflate is replaced by an acetonitrile ligand and the complex displays temperature-

Table 6. Comparison of the Bond Parameters in Iron(II) and Manganese(II) Complexes of N4Py-Type Ligands

complex	M–N _{MeCN}	M–N _{amine}	M–N _{Py}	M–N _{CH₂Py^(Me)}	M–N _{Py^(Me)}	M–N _{CH₂Py}	M–N _Q	∠N _{amine} –M–N _{MeCN}	ref
[Fe ^{II} (N2Py)(N2CH ₂ Py ^{Me})(MeCN)] ²⁺	1.959(3)	1.990(3)	2.004(4)	1.981(3)	2.078(3)	2.083(4)	–	167.55(13)	72
[Fe ^{II} (N4Py ^{Me})(MeCN)] ²⁺ (1b)	1.889(10)	1.977(8)	–	–	2.045(8)	2.043(8)	1.982(9)	178.6(4)	this work
[Fe ^{II} (N2Py2Q)(MeCN)] ²⁺	1.954(6)	2.020(4)	2.019(4)	2.012(5)	–	–	2.102(5)	166.79(19)	81
[Fe ^{II} (N4Py)(MeCN)] ²⁺	1.915(3)	1.961(3)	1.976(3)	1.967(3)	–	–	1.968(3)	177.32(11)	71
[Mn ^{II} (N4Py ^{Me})(MeCN)] ²⁺	2.146(2)	2.244(2)	–	–	2.329(2)	2.317(2)	–	173.02(10)	81

Table 7. Catalytic Activities of $[\text{Fe}^{\text{IV}}(\text{O})(\text{N4Py}^{\text{Me2}})]^{2+}$ (**2**) and $[\text{Fe}^{\text{IV}}(\text{O})(\text{N4Py})]^{2+}$ Towards Various Substrates

substrate (mmol)	product	$[\text{Fe}^{\text{IV}}(\text{O})(\text{N4Py}^{\text{Me2}})]^{2+}$ (2)				$[\text{Fe}^{\text{IV}}(\text{O})(\text{N4Py})]^{2+}$			
		TON ^a	efficiency ^b (%)	A/K ^c	3°/2° ^d	TON ^a	efficiency ^b (%)	A/K ^c	3°/2° ^d
cyclohexane (5)	cyclohexanol	1.9	26	2.7	–	0.3	10	0.4	–
	cyclohexanone	0.7				0.7			
adamantane (0.25)	1- adamantanol	1.9	22	–	22	2.6	32	–	14
	2- adamantanol	0.1				0.1			
toluene (0.5)	2- adamantanone	0.2				0.5			
	benzaldehyde	0.6	6.0	–	–	0.3	2.7	–	–
9,10-DHA (0.25)	anthracene	8.3	83	–	–	7.0	70	–	–
ethylbenzene (0.5)	1-phenylethanol	0.3	9	–	–	0.3	9	–	–
	acetophenone	0.6				0.6			
fluorene (0.25)	fluorenone	2.6	26	–	–	0.9	9	–	–
1,4-CHD (0.5)	benzene	0.6	6	–	–	0.5	5	–	–
1-octene (0.5)	1-octene oxide	3.4	34	–	–	0.2	2	–	–
cyclohexene (5)	cyclohexenol	6.9	89	3.4	–	5.2	83	1.7	–
	cyclohexenone	2.0				3.1			
benzyl alcohol (0.5)	benzaldehyde	4.3	43	–	–	3.6	36	–	–
thioanisole (0.5)	thioanisole oxide	1.1	11	–	–	1.0	10	–	–

^aTurnover number (TON) = mol of product/mol of catalyst. ^bEfficiency (%) = moles of total products/mol of oxidant × 100. ^cA/K = (mol of alcohol)/(mol of ketone). ^dRatio of tertiary alcohol to secondary alcohol (3°/2°) = 3[1-adamantanol/2-adamantanol + 2-adamantanone].

dependent spin crossover. The iron(II) complex reacts with *m*-CPBA or oxone in acetonitrile to generate an *S* = 1 high-valent iron-oxo species, $[\text{Fe}^{\text{IV}}(\text{O})(\text{N4Py}^{\text{Me2}})]^{2+}$ (**2**), exhibiting a characteristic absorption band at 740 nm. The steric hindrance engendered by the 6-Me substituents on the pyridine rings results in weakening of the ligand field of the N4Py^{Me2} ligand in the equatorial plane. The iron-oxo species is relatively unstable with a half-life ($t_{1/2}$) of only 14 min at ambient temperature. Complex **2** is one of the most reactive oxo transfer agents among the reported iron(IV)-oxo complexes of pyridine-rich N5 ligands. In addition, the high-valent iron complex is capable of oxygenating relatively strong C–H bonds of aliphatic substrates including that of cyclohexane (C–H BDE 99.3 kcal/mol). For cyclohexane oxidation, a 10-fold increase in the reactivity is observed with respect to that of the parent N4Py ligand. Surprisingly, complex **2** is less reactive than $[\text{Fe}^{\text{IV}}(\text{O})(\text{N4Py})]^{2+}$ toward substrates with weak C–H bonds (<86 kcal/mol; 9,10-dihydroanthracene, 1,4-cyclohexadiene). In the oxidation of toluene, the intermediate **2** shows a KIE value of 14, clearly indicating the C–H bond abstraction by the iron-oxo species being the rate-limiting step. DFT calculations on the HAT reactions with cyclohexane reveal a lower triplet-quintet splitting in case of **2** compared to parent $[\text{Fe}^{\text{IV}}(\text{O})(\text{N4Py})]^{2+}$ and support the involvement of the quintet transition state in the reaction pathway, in agreement with the two-state reactivity concept. Moreover, the complex displays catalytic OAT and HAT transfer reactivity, albeit with moderate activity.

EXPERIMENTAL SECTION

All chemicals and reagents were obtained from commercial sources and were used without further purification unless otherwise noted. Solvents were distilled and dried before use. Preparation and handling of air-sensitive materials were carried out under an inert atmosphere in a glovebox. Fourier transform infrared spectroscopy on KBr pellets was performed on a Shimadzu FT-IR 8400S instrument. Elemental analyses were performed on a PerkinElmer 2400 series II CHN analyzer. Electro-spray ionization (ESI) mass spectra were recorded with a Waters QTOF Micro YA263 instrument. Solution electronic spectra (single and time-dependent) were measured on an Agilent 8453 diode array spectrophotometer. All room-temperature NMR

spectra were collected on a Bruker Avance 500 MHz spectrometer. ⁵⁷Fe Mössbauer spectra were recorded with a ⁵⁷Co source in a Rh matrix using an alternating constant acceleration Wissel Mössbauer spectrometer operated in the transmission mode and equipped with a Janis closed-cycle helium cryostat. Isomer shifts are given relative to iron metal at ambient temperature. Simulation of the experimental data was performed with the *Mfit* program (E. Bill, Max-Planck Institute for Chemical Energy Conversion, Mülheim/Ruhr, Germany). Temperature-dependent magnetic susceptibility measurements were carried out with a Quantum-Design MPMS-XL-5 SQUID magnetometer equipped with a 5 T magnet in the range from 2 to 295 K at a magnetic field of 0.5 T. GC-MS measurements were carried out with a PerkinElmer Clarus 680 GC and SQ8T MS, using Elite 5 MS (30 m × 0.25 mm × 0.25 μm) column with maximum temperature set at 300 °C. The labeling experiment was carried out with H₂O¹⁸ (98 atom %) from Icon Services Inc.

Synthesis. Bis(6-methylpyridin-2-yl)methanone, bis(6-methylpyridin-2-yl)methanone oxime, and bis(6-methylpyridin-2-yl)-methanamine were prepared according to the procedures reported in literature.⁶⁸ **Caution!** Although no problem was encountered during the synthesis of the complex, perchlorate salts are potentially explosive and should be handled with care!

Ligand N4Py^{Me2}. To a mixture of bis(6-methylpyridin-2-yl)-methanamine (0.50 g, 2.35 mmol) and sodium triacetoxyborohydride (3.44 g, 16.2 mmol) in dichloromethane (50 mL) was added pyridine-2-carboxaldehyde (0.47 mL, 4.9 mmol). The mixture was allowed to stir for 48 h at ambient temperature. Subsequently, a saturated aqueous sodium hydrogen carbonate solution was added, followed by stirring for an additional 1 h. The organic product was then extracted with ethyl acetate (3 × 50 mL). The combined organic extracts were dried over Na₂SO₄ and evaporated to dryness to yield pale yellow oil. Yield: 0.45 g (48%). ¹H NMR (500 MHz, DMSO-*d*₆, 298 K): δ(ppm) 8.42 (d, 2H), 7.80–7.69 (m, 4H), 7.57 (d, 2H), 7.40 (d, 2H), 7.18 (t, 2H), 7.1 (d, 2H), 5.15 (s, 1H), 3.84 (s, 4H), 2.39 (s, 6H). ESI-MS (+ve ion mode, acetonitrile): *m/z* = 396.2 (100%, [M + H]⁺), 418.2 (85%, [M + Na]⁺), 434.2 (20%, [M + K]⁺).

$[\text{Fe}^{\text{II}}(\text{N4Py}^{\text{Me2}})(\text{OTf})](\text{OTf})$ (1**).** Fe(OTf)₂·2MeCN (0.11 g, 0.25 mmol) was added to a dichloromethane solution (5 mL) of the ligand (0.10 g, 0.25 mmol), and the resulting solution was allowed to stir for 6 h under nitrogen atmosphere. The solvent was then removed completely under vacuum, and the residue was washed thoroughly with a mixture of dichloromethane and diethyl ether (1:5) to isolate a light yellow solid. Yield: 0.12 g (58%). Anal. calcd for **1**·CH₂Cl₂·C₂₈H₂₇Cl₂F₆FeN₅O₆S₂ (834.42 g/mol): C, 40.30; H, 3.26; N 8.39;

Found: C 40.06, H 3.35, N 8.06. ESI-MS (+ve ion mode in CH₃CN): $m/z = 225.6$ (100%) [Fe(N4Py^{Me2})²⁺]. UV-vis (CH₃CN): λ_{\max} (ϵ , M⁻¹cm⁻¹); 455 nm (sh), 430 nm (sh), and 360 nm (1200). ¹H NMR (500 MHz in CD₃CN): δ (ppm) 69.2 (Py- α -H), 55.2 (Py-CH₂), 51.3, 49.5 (Py-H β and Py-H β'), 36.3 (Py-H γ), 23.5 (Me-Py-H β and Me-Py-H β'), 13.5 (Me-Py-H α), 7.3 (N-CH), -25.1 (Me-Py-CH₃). X-ray quality single crystals of [Fe(N4Py^{Me2})(CH₃CN)](ClO₄)₂ (**1b**) were grown by recrystallization of the complex (isolated from the reaction of iron(II) perchlorate hydrate and N4Py^{Me2} in acetonitrile) from a solvent mixture of acetonitrile and diethyl ether.

Generation of [Fe^{IV}(O)(N4Py^{Me2})]²⁺ (2**).** To an acetonitrile solution (1 mM) of [Fe^{II}(N4Py^{Me2})(OTf)](OTf) (**1**) was added *m*-CPBA (5 equiv) in acetonitrile at -10 °C. Immediately a pale green species showing an absorption maximum at 740 nm ($\epsilon \sim 220$ M⁻¹cm⁻¹) was observed. The pale green intermediate could also be generated using other oxidants such as PhIO and oxone. When oxone (2 equiv), dissolved in H₂O (50 μ L), was added to an acetonitrile solution **1** (1 mM) at 25 °C, the same species was generated. When excess solid PhIO (20 equiv) was used to generate the green species at -40 °C, a relatively low yield of **2** was observed.

Hydrogen-Atom-Transfer Reactions. Kinetic experiments were performed by adding appropriate amounts of substrates (0.01–0.4 M) to 1 mM solution of **2** (generated by addition of 5 equiv of *m*-CPBA) in CH₃CN solution under anaerobic condition. The decay of the band at 740 nm was monitored spectrophotometrically at 25 °C. Rate constants, k_{obs} , were determined by pseudo-first-order fitting of the absorbance decay at 740 nm. Second-order rate constants k_2 were obtained from the slopes of the linear fits of k_{obs} vs concentration of substrates.

Reactions with Thioanisole and 9,10-DHA at -10 °C. To a solution of **2** generated from complex **1** (2 mM in CH₃CN) was added thioanisole or 9,10-DHA (0.01–0.04 M), and the decay of the 740 nm band was monitored. Following the same methodology as described above, second-order rate constants k_2 were obtained.

Isotope Labeling Experiments. The isotope labeling experiment was carried out by adding 20 μ L H₂¹⁸O (98% ¹⁸O-enriched) to an acetonitrile solution of **2** at -10 °C.

Catalysis Experiments. The catalytic oxidation reactions were carried out using oxone (KHSO₅) as oxidant. In a typical experiment, oxone (0.05 mmol dissolved in 50 μ L H₂O) was added to an acetonitrile solution (2 mL) of the complex (0.005 mmol) [Fe^{II}(N4Py^{Me2})(CH₃CN)]²⁺ or [Fe^{II}(N4Py)(CH₃CN)]²⁺ containing appropriate amounts of external substrates (Table 7). The reaction mixture was stirred in air for 1 h at 298 K. To isolate the organic products, the solution at the end of the reaction was passed through a small silica column (to remove Fe-catalyst), followed by washing with ethyl acetate. The ethyl acetate solution was then analyzed directly by GC-MS (with naphthalene as quantification standard). The thioanisole oxidation product was identified by ¹H NMR and quantified using 2,4-di-*tert*-butylphenol as an internal standard.

X-ray Crystallographic Data Collection, Refinement, and Solution of the Structure of 1b. X-ray single-crystal data for **1b** were collected at 223 K using Mo K α ($\lambda = 0.7107$ Å) radiation on a SMART-APEX diffractometer equipped with CCD area detector. Data collection, data reduction, structure solution, and refinement were carried out using the software package of APEX II.⁹⁰ The structure was solved by direct methods and subsequent Fourier analyses and refined by the full-matrix least-squares method based on F^2 with all observed reflections.⁹¹ The non-hydrogen atoms were treated anisotropically.

Crystal Data of 1b. MF = C₂₇H₂₈Cl₂FeN₆O₈, $M_r = 691.30$, monoclinic, space group P2₁/c, $a = 18.312(7)$, $b = 12.860(5)$, $c = 13.500(5)$ Å, $\alpha = 90.00^\circ$, $\beta = 106.411(6)^\circ$, $\gamma = 90.00^\circ$, $V = 3050.0(2)$ Å³, $Z = 4$, $\rho = 1.506$ mg m⁻³, μ Mo-K $\alpha = 0.728$ mm⁻¹, $F(000) = 1424$, GOF = 1.070. A total of 10,806 reflections were collected in the range $1.16 \leq \theta \leq 23.46$, 4399 of which were unique ($R_{\text{int}} = 0.2075$). $R_1(wR_2) = 0.0863$ (0.1924) for 400 parameters and 4399 reflections ($I > 2\sigma(I)$).

Computational Studies. All calculations were performed with the Gaussian 09 program.⁹² Geometry optimizations were performed

using the UBLYP^{93–95} hybrid density functional method in combination with Pople's 6-31++G(d,p) basis set. The 1997 Stuttgart relativistic small-core effective core-potential (Stuttgart RSC 1997 ECP, denoted as SDD)^{96,97} was employed for the core electrons of the Fe center, and the (311111/22111/411/1) basis set was used for its valence electrons. Harmonic vibrational frequency calculations were performed at the same level of theory to characterize the structures as intermediates (all real frequencies) and transition states (one imaginary mode) and also to extract thermo-chemical information. Single point condensed phase calculations were also performed using the CPCM⁹⁸ solvent model at the uB3LYP/6-31++G(d,p)/Fe(SDD) level of theory with empirical dispersion added to it (B3LYP-D3) using the universal force field (UFF) radii. The dielectric constant in the CPCM calculations was set to 35.688 to simulate acetonitrile.

■ ASSOCIATED CONTENT

📄 Supporting Information

The Supporting Information is available free of charge on the ACS Publications website at DOI: 10.1021/acs.inorgchem.8b02577.

Spectroscopic data, DFT optimized coordinates, and crystallographic data in CIF format (PDF)

Accession Codes

CCDC 1824770 contains the supplementary crystallographic data for this paper. These data can be obtained free of charge via www.ccdc.cam.ac.uk/data_request/cif, or by emailing data_request@ccdc.cam.ac.uk, or by contacting The Cambridge Crystallographic Data Centre, 12 Union Road, Cambridge CB2 1EZ, UK; fax: +44 1223 336033.

■ AUTHOR INFORMATION

Corresponding Authors

*E-mail: ictkp@iacs.res.in (T.K.P.).

*E-mail: icrs@iacs.res.in (R.S.).

ORCID

Franz Meyer: 0000-0002-8613-7862

Tapan Kanti Paine: 0000-0002-4234-1909

Present Address

^{||}Department of Chemistry, Taras Shevchenko National University of Kyiv, 64/13Volodymyrska Street, City of Kyiv, Ukraine, 01601

Notes

The authors declare no competing financial interest.

■ ACKNOWLEDGMENTS

The authors gratefully acknowledge the Swedish Research Links Programme of the Swedish Research Council (T.K.P., E.N.), and the Science and Engineering Research Board (SERB) (T.K.P. and R.S.) for financial support. R.S. thanks the Council of Scientific and Industrial Research (CSIR), India, for a research associateship. The authors thank Mr. Sridhar Banerjee for his help with Mössbauer studies and Dr. Arup Sinha for assistance in analysis of crystal structure data.

■ REFERENCES

- (1) Solomon, E. I.; Brunold, T. C.; Davis, M. I.; Kemsley, J. N.; Lee, S.-K.; Lehnert, N.; Neese, F.; Skulan, A. J.; Yang, Y.-S.; Zhou, J. Geometric and Electronic Structure/Function Correlations in Non-Heme Iron Enzymes. *Chem. Rev.* **2000**, *100*, 235–349.
- (2) Hausinger, R. P. Fe(II)- α -Ketoglutarate-Dependent Hydroxylases and Related Enzymes. *Crit. Rev. Biochem. Mol. Biol.* **2004**, *39*, 21–68.

- (3) Costas, M.; Mehn, M. P.; Jensen, M. P.; Que, L., Jr. Oxygen Activation at Mononuclear Nonheme Iron: Enzymes, Intermediates and Models. *Chem. Rev.* **2004**, *104*, 939–986.
- (4) Kovaleva, E. G.; Lipscomb, J. D. Versatility of biological non-heme Fe(II) centers in oxygen activation reactions. *Nat. Chem. Biol.* **2008**, *4*, 186–193.
- (5) Ray, K.; Pfaff, F. F.; Wang, B.; Nam, W. Status of Reactive Nonheme Metal-Oxygen Intermediates in Chemical and Enzymatic Reactions. *J. Am. Chem. Soc.* **2014**, *136*, 13942–13958.
- (6) Sono, M.; Roach, M. P.; Coulter, E. D.; Dawson, J. H. Heme-Containing Oxygenases. *Chem. Rev.* **1996**, *96*, 2841–2888.
- (7) Rittle, J.; Green, M. T. Cytochrome P450 compound I: capture, characterization, and C-H bond activation kinetics. *Science* **2010**, *330*, 933–937.
- (8) Que, L., Jr. The heme paradigm revisited: alternative reaction pathways considered. *JBIC, J. Biol. Inorg. Chem.* **2004**, *9*, 643–690.
- (9) Wallar, B. J.; Lipscomb, J. D. Dioxygen Activation by Enzymes Containing Binuclear Non-Heme Iron Clusters. *Chem. Rev.* **1996**, *96*, 2625–2658.
- (10) Tinberg, C. E.; Lippard, S. J. Dioxygen Activation in Soluble Methane Monooxygenase. *Acc. Chem. Res.* **2011**, *44*, 280–288.
- (11) Lee, S.-K.; Fox, B. G.; Froland, W. A.; Lipscomb, J. D.; Münck, E. A Transient Intermediate of the Methane Monooxygenase Catalytic Cycle Containing an Fe^{IV}Fe^{IV} Cluster. *J. Am. Chem. Soc.* **1993**, *115*, 6450–6451.
- (12) Shu, L.; Nesheim, J. C.; Kauffmann, K.; Münck, E.; Lipscomb, J. D.; Que, L., Jr. An Fe^{IV}O₂ Diamond Core Structure for the Key Intermediate Q of Methane Monooxygenase. *Science* **1997**, *275*, 515–518.
- (13) Penner-Hahn, J. E.; Smith Eble, K.; McMurry, T. J.; Renner, M.; Balch, A. L.; Groves, J. T.; Dawson, J. H.; Hodgson, K. O. Structural Characterization of Horseradish Peroxidase Using EXAFS Spectroscopy: Evidence for Fe=O Ligation in Compounds I and II. *J. Am. Chem. Soc.* **1986**, *108*, 7819–7825.
- (14) Krebs, C.; Fujimori, D. G.; Walsh, C. T.; Bollinger, J. M., Jr. Non-Heme Fe(IV)–Oxo Intermediates. *Acc. Chem. Res.* **2007**, *40*, 484–492.
- (15) Price, J. C.; Barr, E. W.; Tirupati, B.; Bollinger, J. M., Jr.; Krebs, C. The First Direct Characterization of a High-Valent Iron Intermediate in the Reaction of an α -Ketoglutarate-Dependent Dioxygenase: A High-Spin Fe(IV) Complex in Taurine/ α -Ketoglutarate Dioxygenase (TauD) from *Escherichia coli*. *Biochemistry* **2003**, *42*, 7497–7508.
- (16) Proshlyakov, D. A.; Henshaw, T. F.; Monterosso, G. R.; Ryle, M. J.; Hausinger, R. P. Direct Detection of Oxygen Intermediates in the Non-Heme Fe Enzyme Taurine/ α -Ketoglutarate Dioxygenase. *J. Am. Chem. Soc.* **2004**, *126*, 1022–1023.
- (17) Riggs-Gelasco, P. J.; Price, J. C.; Guyer, R. B.; Brehm, J. H.; Barr, E. W.; Bollinger, J. M., Jr.; Krebs, C. EXAFS Spectroscopic Evidence for an Fe=O Unit in the Fe(IV) Intermediate Observed during Oxygen Activation by Taurine: α -Ketoglutarate Dioxygenase. *J. Am. Chem. Soc.* **2004**, *126*, 8108–8109.
- (18) Sinnecker, S.; Svensen, N.; Barr, E. W.; Ye, S.; Bollinger, J. M., Jr.; Neese, F.; Krebs, C. Spectroscopic and Computational Evaluation of the Structure of the High-Spin Fe(IV)-Oxo Intermediates in Taurine: α -Ketoglutarate Dioxygenase from *Escherichia coli* and Its His99Ala Ligand Variant. *J. Am. Chem. Soc.* **2007**, *129*, 6168–6179.
- (19) Kal, S.; Que, L., Jr. Dioxygen activation by nonheme iron enzymes with the 2-His-1-carboxylate facial triad that generate high-valent oxoiron oxidants. *JBIC, J. Biol. Inorg. Chem.* **2017**, *22*, 339–365.
- (20) Grapperhaus, C. A.; Mienert, B.; Bill, E.; Weyhermüller, T.; Wieghardt, K. Mononuclear (Nitrido)iron(V) and (Oxo)iron(IV) Complexes via Photolysis of [(cyclam-acetato)Fe^{III}(N₃)]⁺ and Ozonolysis of [(cyclam-acetato)Fe^{III}(O₃SCF₃)]⁺ in Water/Acetone Mixtures. *Inorg. Chem.* **2000**, *39*, 5306–5317.
- (21) Rohde, J.-U.; In, J. H.; Lim, M. H.; Brennessel, W. W.; Bukowski, M. R.; Stubna, A.; Münck, E.; Nam, W.; Que, L., Jr. Crystallographic and Spectroscopic Evidence for a Nonheme Fe^{IV}=O Complex. *Science* **2003**, *299*, 1037–1039.
- (22) Nam, W. High-Valent Iron(IV)–Oxo Complexes of Heme and Non-Heme Ligands in Oxygenation Reactions. *Acc. Chem. Res.* **2007**, *40*, 522–531.
- (23) Que, L., Jr. The Road to Non-Heme Oxoferryls and Beyond. *Acc. Chem. Res.* **2007**, *40*, 493–500.
- (24) Hohenberger, J.; Ray, K.; Meyer, K. The biology and chemistry of high-valent iron–oxo and iron–nitrido complexes. *Nat. Commun.* **2012**, *3*, 720–733.
- (25) McDonald, A. R.; Que, L., Jr. High-Valent Nonheme Iron-Oxo Complexes: Synthesis, Structure, and Spectroscopy. *Coord. Chem. Rev.* **2013**, *257*, 414–428.
- (26) MacBeth, C. E.; Golombek, A. P.; Young, V. G., Jr.; Yang, C.; Kuczera, K.; Hendrich, M. P.; Borovik, A. S. O₂ Activation by Nonheme Iron Complexes: A Monomeric Fe(III)-Oxo Complex Derived From O₂. *Science* **2000**, *289*, 938–941.
- (27) Tiago de Oliveira, F.; Chanda, A.; Banerjee, D.; Shan, X.; Mondal, S.; Que, L., Jr.; Bominaar, E. L.; Münck, E.; Collins, T. J. Chemical and spectroscopic evidence for an Fe^V-Oxo Complex. *Science* **2007**, *315*, 835–838.
- (28) Van Heuvelen, K. M.; Fiedler, A. T.; Shan, X.; De Hont, R. F.; Meier, K. K.; Bominaar, E. L.; Münck, E.; Que, L., Jr. One-electron oxidation of an oxoiron(IV) complex to form an [O=Fe^V=NR]⁺ center. *Proc. Natl. Acad. Sci. U. S. A.* **2012**, *109*, 11933–11938.
- (29) Serrano-Plana, J.; Oloo, W. N.; Acosta-Rueda, L.; Meier, K. K.; Verdejo, B.; García-España, E.; Basallote, M. G.; Münck, E.; Que, L., Jr.; Company, A.; Costas, M. Trapping a Highly Reactive Nonheme Iron Intermediate That Oxygenates Strong C-H Bonds with Stereoretention. *J. Am. Chem. Soc.* **2015**, *137*, 15833–15842.
- (30) Nam, W.; Lee, Y.-M.; Fukuzumi, S. Tuning Reactivity and Mechanism in Oxidation Reactions by Mononuclear Nonheme Iron(IV)-Oxo Complexes. *Acc. Chem. Res.* **2014**, *47*, 1146–1154.
- (31) Engelmann, X.; Monte-Pérez, I.; Ray, K. Oxidation Reactions with Bioinspired Mononuclear Non-Heme Metal-Oxo Complexes. *Angew. Chem., Int. Ed.* **2016**, *55*, 7632–7649.
- (32) Sastri, C. V.; Lee, J.; Oh, K.; Lee, Y. J.; Lee, J.; Jackson, T. A.; Ray, K.; Hirao, H.; Shin, W.; Halfen, J. A.; Kim, J.; Que, L., Jr.; Shaik, S.; Nam, W. Axial ligand tuning of a nonheme iron(IV)–oxo unit for hydrogen atom abstraction. *Proc. Natl. Acad. Sci. U. S. A.* **2007**, *104*, 19181–19186.
- (33) Kaizer, J.; Klinker, E. J.; Oh, N. Y.; Rohde, J.-U.; Song, W. J.; Stubna, A.; Kim, J.; Nam, W.; Münck, E.; Que, L., Jr. Nonheme Fe^{IV}O Complexes That Can Oxidize the C-H Bonds of Cyclohexane at Room Temperature. *J. Am. Chem. Soc.* **2004**, *126*, 472–473.
- (34) Kleespies, S. T.; Oloo, W. N.; Mukherjee, A.; Que, L., Jr. C–H Bond Cleavage by Bioinspired Nonheme Oxoiron(IV) Complexes, Including Hydroxylation of *n*-Butane. *Inorg. Chem.* **2015**, *54*, 5053–5064.
- (35) Wang, D.; Ray, K.; Collins, M. J.; Farquhar, E. R.; Frisch, J. R.; Gómez, L.; Jackson, T. A.; Kerscher, M.; Waleska, A.; Comba, P.; Costas, M.; Que, L., Jr. Nonheme oxoiron(IV) complexes of pentadentate N5 ligands: spectroscopy, electrochemistry, and oxidative reactivity. *Chem. Sci.* **2013**, *4*, 282–291.
- (36) Seo, M. S.; Kim, N. H.; Cho, K.-B.; So, J. E.; Park, S. K.; Clemancey, M.; Garcia-Serres, R.; Latour, J.-M.; Shaik, S.; Nam, W. A mononuclear nonheme iron(IV)-oxo complex which is more reactive than cytochrome P450 model compound I. *Chem. Sci.* **2011**, *2*, 1039–1045.
- (37) Lim, M. H.; Rohde, J.-U.; Stubna, A.; Bukowski, M. R.; Costas, M.; Ho, R. Y. N.; Münck, E.; Nam, W.; Que, L., Jr. An Fe^{IV}=O Complex of a Tetradentate Tripodal Nonheme Ligand. *Proc. Natl. Acad. Sci. U. S. A.* **2003**, *100*, 3665–3670.
- (38) Klinker, E. J.; Kaizer, J.; Brennessel, W. W.; Woodrum, N. L.; Cramer, C. J.; Que, L., Jr. Structures of Nonheme Oxoiron(IV) Complexes from X-ray Crystallography, NMR Spectroscopy, and DFT Calculations. *Angew. Chem., Int. Ed.* **2005**, *44*, 3690–3694.
- (39) Bautz, J.; Comba, P.; de Laorden, C. L.; Menzel, M.; Rajaraman, G. Biomimetic High-Valent Non-Heme Iron Oxidants for the *cis*-Dihydroxylation and Epoxidation of Olefins. *Angew. Chem., Int. Ed.* **2007**, *46*, 8067–8070.

- (40) Chanda, A.; Shan, X.; Chakrabarti, M.; Ellis, W. C.; Popescu, D. L.; Tiago de Oliveira, F.; Wang, D.; Que, L., Jr.; Collins, T. J.; Münck, E.; Bominaar, E. L. (TAML)Fe^{IV}=O Complex in Aqueous Solution: Synthesis and Spectroscopic and Computational Characterization. *Inorg. Chem.* **2008**, *47*, 3669–3678.
- (41) Ray, K.; England, J.; Fiedler, A. T.; Martinho, M.; Münck, E.; Que, L., Jr. An Inverted and More Oxidizing Isomer of [Fe^{IV}(O)-(tmc)(NCCH₃)₂]²⁺. *Angew. Chem., Int. Ed.* **2008**, *47*, 8068–8071.
- (42) Thibon, A.; England, J.; Martinho, M.; Young, V. G., Jr.; Frisch, J. R.; Guillot, R.; Girerd, J.-J.; Münck, E.; Que, L., Jr.; Banse, F. Proton- and Reductant-Assisted Dioxygen Activation by a Nonheme Iron(II) Complex to Form an Oxoiron(IV) Intermediate. *Angew. Chem., Int. Ed.* **2008**, *47*, 7064–7067.
- (43) Kotani, H.; Suenobu, T.; Lee, Y.-M.; Nam, W.; Fukuzumi, S. Photocatalytic Generation of a Non-Heme Oxoiron(IV) Complex with Water as an Oxygen Source. *J. Am. Chem. Soc.* **2011**, *133*, 3249–3251.
- (44) Company, A.; Prat, I.; Frisch, J. R.; Mas-Ballesté, R.; Güell, M.; Juhász, G.; Ribas, X.; Münck, E.; Luis, J. M.; Que, L., Jr.; Costas, M. Modeling the cis-Oxo-Labile Binding Site Motif of Non-Heme Iron Oxygenases: Water Exchange and Oxidation Reactivity of a Non-Heme Iron(IV)-Oxo Compound Bearing a Tripodal Tetradentate Ligand. *Chem. - Eur. J.* **2011**, *17*, 1622–1634.
- (45) Martinho, M.; Banse, F.; Bartoli, J.-F.; Mattioli, T. A.; Battioni, P.; Horner, O.; Bourcier, S.; Girerd, J.-J. New Example of a Non-Heme Mononuclear Iron(IV) Oxo Complex. Spectroscopic Data and Oxidation Activity. *Inorg. Chem.* **2005**, *44*, 9592–9596.
- (46) Meyer, S.; Klawitter, I.; Demeshko, S.; Bill, E.; Meyer, F. A Tetracarbene–Oxoiron(IV) Complex. *Angew. Chem., Int. Ed.* **2013**, *52*, 901–905.
- (47) Ye, W.; Ho, D. M.; Friedle, S.; Palluccio, T. D.; Rybak-Akimova, E. V. Role of Fe(IV)-Oxo Intermediates in Stoichiometric and Catalytic Oxidations Mediated by Iron Pyridine-Azamacrocycles. *Inorg. Chem.* **2012**, *51*, 5006–5021.
- (48) Vad, M. S.; Lennartson, A.; Nielsen, A.; Harmer, J.; McGrady, J. E.; Frandsen, C.; Mørup, S.; McKenzie, C. J. An aqueous non-heme Fe(IV) oxo complex with a basic group in the second coordination sphere. *Chem. Commun.* **2012**, *48*, 10880–10882.
- (49) Chantarojsiri, T.; Sun, Y.; Long, J. R.; Chang, C. J. Water-Soluble Iron(IV)-Oxo Complexes Supported by Pentapyridine Ligands: Axial Ligand Effects on Hydrogen Atom and Oxygen Atom Transfer Reactivity. *Inorg. Chem.* **2015**, *54*, 5879–5887.
- (50) Ye, S.; Kupper, C.; S, M.; Andris, E.; Navrátil, R.; Krahe, O.; Mondal, B.; Atanasov, M.; Bill, E.; Roithová, J.; Meyer, F.; Neese, F. Magnetic Circular Dichroism Evidence for an Unusual Electronic Structure of a Tetracarbene–Oxoiron(IV) Complex. *J. Am. Chem. Soc.* **2016**, *138*, 14312–14325.
- (51) Kupper, C.; Mondal, B.; Serrano-Plana, J.; Klawitter, I.; Neese, F.; Costas, M.; Ye, S.; Meyer, F. Nonclassical Single-State Reactivity of an Oxo-Iron(IV) Complex Confined to Triplet Pathways. *J. Am. Chem. Soc.* **2017**, *139*, 8939–8949.
- (52) Bigi, J. P.; Harman, W. H.; Lassalle-Kaiser, B.; Robles, D. M.; Stich, T. A.; Yano, J.; Britt, R. D.; Chang, C. J. A High-Spin Iron(IV)-Oxo Complex Supported by a Trigonal Nonheme Pyrrolide Platform. *J. Am. Chem. Soc.* **2012**, *134*, 1536–1542.
- (53) Pestovsky, O.; Stoian, S.; Bominaar, E. L.; Shan, X.; Münck, E.; Que, L., Jr.; Bakac, A. Aqueous Fe^{IV}=O: Spectroscopic Identification and Oxo-Group Exchange. *Angew. Chem., Int. Ed.* **2005**, *44*, 6871–6874.
- (54) England, J.; Martinho, M.; Farquhar, E. R.; Frisch, J. R.; Bominaar, E. L.; Münck, E.; Que, L., Jr. A Synthetic High-Spin Oxoiron(IV) Complex: Generation, Spectroscopic Characterization, and Reactivity. *Angew. Chem., Int. Ed.* **2009**, *48*, 3622–3626.
- (55) England, J.; Guo, Y.; Farquhar, E. R.; Young, V. G., Jr.; Münck, E.; Que, L., Jr. The Crystal Structure of a High-Spin Oxoiron(IV) Complex and Characterization of Its Self-Decay Pathway. *J. Am. Chem. Soc.* **2010**, *132*, 8635–8644.
- (56) Lacy, D. C.; Gupta, R.; Stone, K. L.; Greaves, J.; Ziller, J. W.; Hendrich, M. P.; Borovik, A. S. Formation, Structure, and EPR Detection of a High Spin Fe^{IV}-Oxo Species Derived from Either an Fe^{III}-Oxo or Fe^{III}-OH Complex. *J. Am. Chem. Soc.* **2010**, *132* (35), 12188–12190.
- (57) Biswas, A. N.; Puri, M.; Meier, K. K.; Oloo, W. N.; Rohde, G. T.; Bominaar, E. L.; Münck, E.; Que, L., Jr. Modeling TauD-J: A High-Spin Nonheme Oxoiron(IV) Complex with High Reactivity toward C–H Bonds. *J. Am. Chem. Soc.* **2015**, *137*, 2428–2431.
- (58) England, J.; Guo, Y.; Van Heuvelen, K. M.; Cranswick, M. A.; Rohde, G. T.; Bominaar, E. L.; Münck, E.; Que, L., Jr. A More Reactive Trigonal-Bipyramidal High-Spin Oxoiron(IV) Complex with a cis-Labile Site. *J. Am. Chem. Soc.* **2011**, *133*, 11880–11883.
- (59) Puri, M.; Que, L., Jr. Toward the Synthesis of More Reactive S = 2 Non-Heme Oxoiron(IV) Complexes. *Acc. Chem. Res.* **2015**, *48*, 2443–2452.
- (60) Bae, S. H.; Seo, M. S.; Lee, Y.-M.; Cho, K.-B.; Kim, W.-S.; Nam, W. Mononuclear Nonheme High-Spin (S = 2) versus Intermediate-Spin (S = 1) Iron(IV)–Oxo Complexes in Oxidation Reactions. *Angew. Chem., Int. Ed.* **2016**, *55*, 8027–8031.
- (61) Hirao, H.; Kumar, D.; Que, L., Jr.; Shaik, S. Two-State Reactivity in Alkane Hydroxylation by Non-Heme Iron–Oxo Complexes. *J. Am. Chem. Soc.* **2006**, *128*, 8590–8606.
- (62) Shaik, S.; Chen, H.; Janardanan, D. Exchange-enhanced reactivity in bond activation by metal–oxo enzymes and synthetic reagents. *Nat. Chem.* **2011**, *3*, 19–27.
- (63) Sahu, S.; Widger, L. R.; Quesne, M. G.; de Visser, S. P.; Matsumura, H.; Moëne-Loccoz, P.; Siegler, M. A.; Goldberg, D. P. Secondary Coordination Sphere Influence on the Reactivity of Nonheme Iron(II) Complexes: An Experimental and DFT Approach. *J. Am. Chem. Soc.* **2013**, *135*, 10590–10593.
- (64) Sahu, S.; Quesne, M. G.; Davies, C. G.; Dürr, M.; Ivanović-Burmazović, I.; Siegler, M. A.; Jameson, G. N. L.; de Visser, S. P.; Goldberg, D. P. Direct Observation of a Nonheme Iron(IV)–Oxo Complex That Mediates Aromatic C–F Hydroxylation. *J. Am. Chem. Soc.* **2014**, *136*, 13542–13545.
- (65) Sahu, S.; Zhang, B.; Pollock, C. J.; Dürr, M.; Davies, C. G.; Confer, A. M.; Ivanović-Burmazović, I.; Siegler, M. A.; Jameson, G. N. L.; Krebs, C.; Goldberg, D. P. Aromatic C–F Hydroxylation by Nonheme Iron(IV)–Oxo Complexes: Structural, Spectroscopic, and Mechanistic Investigations. *J. Am. Chem. Soc.* **2016**, *138*, 12791–12802.
- (66) Mitra, M.; Nimir, H.; Demeshko, S.; Bhat, S. S.; Malinkin, S. O.; Haukka, M.; Lloret-Fillol, J.; Lisensky, G. C.; Meyer, F.; Shteinman, A. A.; Browne, W. R.; Hrovat, D. A.; Richmond, M. G.; Costas, M.; Nordlander, E. Nonheme Fe(IV) Oxo Complexes of Two New Pentadentate Ligands and Their Hydrogen-Atom and Oxygen-Atom Transfer Reactions. *Inorg. Chem.* **2015**, *54*, 7152–7164.
- (67) Rasheed, W.; Draksharapu, A.; Banerjee, S.; Young, V. G., Jr.; Fan, R.; Guo, Y.; Ozerov, M.; Nehrkor, J.; Krzystek, J.; Telsler, J.; Que, L., Jr. Crystallographic evidence for a sterically induced ferryl tilt in a non-heme oxoiron(IV) complex that makes it a better oxidant. *Angew. Chem., Int. Ed.* **2018**, *57*, 9387–9391.
- (68) Chatterjee, S.; Sheet, D.; Paine, T. K. Catalytic and regioselective extradiol cleavage of catechol by a biomimetic iron complex. *Chem. Commun.* **2013**, *49*, 10251–10253.
- (69) Lubben, M.; Meetsma, A.; Wilkinson, E. C.; Feringa, B.; Que, L., Jr. Nonheme Iron Centers in Oxygen Activation: Characterization of an Iron(III) Hydroperoxide Intermediate. *Angew. Chem., Int. Ed. Engl.* **1995**, *34*, 1512–1514.
- (70) Britovsek, G. J. P.; England, J.; White, A. J. P. Non-heme Iron(II) Complexes Containing Tripodal Tetradentate Nitrogen Ligands and Their Application in Alkane Oxidation Catalysis. *Inorg. Chem.* **2005**, *44*, 8125–8134.
- (71) Roelfes, G.; Lubben, M.; Chen, K.; Ho, R. Y. N.; Meetsma, A.; Genseberger, S.; Hermant, R. M.; Hage, R.; Mandal, S. K.; Young, V. G., Jr.; Zang, Y.; Kooijman, H.; Spek, A. L.; Que, L., Jr.; Feringa, B. L. Iron Chemistry of a Pentadentate Ligand That Generates a Metastable Fe^{III}-OOH Intermediate. *Inorg. Chem.* **1999**, *38*, 1929–1936.

- (72) Spek, A. L.; Schoondergang, M. F. J.; Feringa, B. L., CSD Communication. *Private Communication*, 2004.
- (73) Zhang, Y.; Kim, J.; Dong, Y.; Wilkinson, E. C.; Appelman, E. H.; Que, L., Jr. Models for Nonheme Iron Intermediates: Structural Basis for Tuning the Spin States of Fe(TPA) Complexes. *J. Am. Chem. Soc.* **1997**, *119*, 4197–4205.
- (74) Decker, A.; Rohde, J.-U.; Que, L., Jr.; Solomon, E. I. Spectroscopic and Quantum Chemical Characterization of the Electronic Structure and Bonding in a Non-Heme Fe^{IV}=O Complex. *J. Am. Chem. Soc.* **2004**, *126*, 5378–5379.
- (75) Bautz, J.; Bukowski, M. R.; Kerscher, M.; Stubna, A.; Comba, P.; Lienke, A.; Münck, E.; Que, L., Jr. Formation of an Aqueous Oxoiron(IV) Complex at pH 2–6 from a Nonheme Iron(II) Complex and H₂O₂. *Angew. Chem., Int. Ed.* **2006**, *45*, 5681–5684.
- (76) McDonald, A. R.; Guo, Y.; Vu, V. V.; Bominaar, E. L.; Münck, E.; Que, L., Jr. A mononuclear carboxylate-rich oxoiron(IV) complex: a structural and functional mimic of TauD intermediate [J]. *Chem. Sci.* **2012**, *3*, 1680–1693.
- (77) Seo, M. S.; In, J.-H.; Kim, S. O.; Oh, N. Y.; Hong, J.; Kim, J.; Que, L., Jr.; Nam, W. Direct Evidence for Oxygen-Atom Exchange between Nonheme Oxoiron(IV) Complexes and Isotopically Labeled Water. *Angew. Chem., Int. Ed.* **2004**, *43*, 2417–2420.
- (78) Comba, P.; Fukuzumi, S.; Kotani, H.; Wunderlich, S. Electron-Transfer Properties of an Efficient Nonheme Iron Oxidation Catalyst with a Tetradentate Bispidine Ligand. *Angew. Chem., Int. Ed.* **2010**, *49*, 2622–2625.
- (79) Klinker, E. J.; Shaik, S.; Hirao, H.; Que, L., Jr. A Two-State Reactivity Model Explains Unusual Kinetic Isotope Effect Patterns in C-H Bond Cleavage by Nonheme Oxoiron(IV) Complexes. *Angew. Chem., Int. Ed.* **2009**, *48*, 1291–1295.
- (80) Monte Pérez, I.; Engelmann, X.; Lee, Y.-M.; Yoo, M.; Kumaran, E.; Farquhar, E. R.; Bill, E.; England, J.; Nam, W.; Swart, M.; Ray, K. A Highly Reactive Oxoiron(IV) Complex Supported by a Bioinspired N₃O Macrocyclic Ligand. *Angew. Chem., Int. Ed.* **2017**, *56*, 14384–14388.
- (81) Sinha, A.; Singh, R.; Yiga, S.; Wendt, O.; Paine, T. K.; Nordlander, E., unpublished work.
- (82) Decker, A.; Rohde, J.-U.; Klinker, E. J.; Wong, S. D.; Que, L., Jr.; Solomon, E. I. Spectroscopic and Quantum Chemical Studies on Low-Spin Fe^{IV}O Complexes: Fe–O Bonding and Its Contributions to Reactivity. *J. Am. Chem. Soc.* **2007**, *129*, 15983–15996.
- (83) Hirao, H.; Que, L., Jr.; Nam, W.; Shaik, S. A Two-State Reactivity Rationale for Counterintuitive Axial Ligand Effects on the C-H Activation Reactivity of Nonheme Fe^{IV}=O Oxidants. *Chem. - Eur. J.* **2008**, *14*, 1740–1756.
- (84) Bell, C. B., III; Wong, S. D.; Xiao, Y.; Klinker, E. J.; Tenderholt, A. L.; Smith, M. C.; Rohde, J.-U.; Que, L., Jr.; Cramer, S. P.; Solomon, E. I. A Combined NRVs and DFT Study of Fe^{IV}=O Model Complexes: a Diagnostic Method for the Elucidation of Non-Heme Iron Enzyme Intermediates. *Angew. Chem., Int. Ed.* **2008**, *47*, 9071–9074.
- (85) Snyder, B. E. R.; Böttger, L. H.; Bols, M. L.; Yan, J. J.; Rhoda, H. M.; Jacobs, A. B.; Hu, M. Y.; Zhao, J.; Alp, E. E.; Hedman, B.; Hodgson, K. O.; Schoonheydt, R. A.; Sels, B. F.; Solomon, E. I. Structural characterization of a non-heme iron active site in zeolites that hydroxylates methane. *Proc. Natl. Acad. Sci. U. S. A.* **2018**, *115*, 4565–4570.
- (86) Groves, J. T.; Nemo, T. E. Aliphatic Hydroxylation Catalyzed by Iron Porphyrin Complexes. *J. Am. Chem. Soc.* **1983**, *105*, 6243–6248.
- (87) Nam, W. Synthetic Mononuclear Nonheme Iron–Oxygen Intermediates. *Acc. Chem. Res.* **2015**, *48*, 2415–2423.
- (88) Cho, K.-B.; Wu, X.; Lee, Y.-M.; Kwon, Y. H.; Shaik, S.; Nam, W. Evidence for an alternative to the oxygen rebound mechanism in C-H bond activation by nonheme Fe^{IV}O complexes. *J. Am. Chem. Soc.* **2012**, *134*, 20222–20225.
- (89) Cho, K.-B.; Hirao, H.; Shaik, S.; Nam, W. To rebound or dissociate? This is the mechanistic question in C–H hydroxylation by heme and nonheme metal–oxo complexes. *Chem. Soc. Rev.* **2016**, *45*, 1197–1210.
- (90) APEX 2, v2.1.0; Bruker AXS: Madison, WI, 2006.
- (91) Sheldrick, G. M. *SHELXL-97, Program for crystal structure refinement*; University of Göttingen: Göttingen, Germany, 1997.
- (92) Frisch, M. J.; Trucks, G. W.; Schlegel, H. B.; Scuseria, G. E.; Robb, M. A.; Cheeseman, J. R.; Scalmani, G.; Barone, V.; Mennucci, B.; Petersson, G. A.; Nakatsuji, H.; Caricato, M.; Li, X.; Hratchian, H. P.; Izmaylov, A. F.; Bloino, J.; Zheng, G.; Sonnenberg, J. L.; Hada, M.; Ehara, M.; Toyota, K.; Fukuda, R.; Hasegawa, J.; Ishida, M.; Nakajima, T.; Honda, Y.; Kitao, O.; Nakai, H.; Vreven, T.; Montgomery, J. A., Jr.; Peralta, J. E., Jr.; Ogliaro, F.; Bearpark, M.; Heyd, J. J.; Brothers, E.; Kudin, K. N.; Staroverov, V. N.; Kobayashi, R.; Normand, J.; Raghavachari, K.; Rendell, A.; Burant, J. C.; Iyengar, S. S.; Tomasi, J.; Cossi, M.; Rega, N.; Millam, J. M.; Klene, M.; Knox, J. E.; Cross, J. B.; Bakken, V.; Adamo, C.; Jaramillo, J.; Gomperts, R.; Stratmann, R. E.; Yazyev, O.; Austin, A. J.; Cammi, R.; Pomelli, C.; Ochterski, J. W.; Martin, R. L.; Morokuma, K.; Zakrzewski, V. G.; Voth, G. A.; Salvador, P.; Dannenberg, J. J.; Dapprich, S.; Daniels, A. D.; Farkas, Ö.; Foresman, J. B.; Ortiz, J. V.; Cioslowski, J.; Fox, D. J. *Gaussian 09*, Revision A.1; Gaussian, Inc.: Wallingford, CT, 2009.
- (93) Lee, C.; Yang, W.; Parr, R. G. Development of the Colle-Salvetti correlation-energy formula into a functional of the electron density. *Phys. Rev. B: Condens. Matter Mater. Phys.* **1988**, *37*, 785–789.
- (94) Becke, A. D. Density-functional thermochemistry. I. The effect of the exchange-only gradient correction. *J. Chem. Phys.* **1992**, *96*, 2155–2160.
- (95) Becke, A. D. Density-functional thermochemistry. II. The effect of the Perdew-Wang generalized-gradient correlation correction. *J. Chem. Phys.* **1992**, *97*, 9173–9177.
- (96) Kaupp, M.; Schleyer, P. v. R.; Stoll, H.; Preuss, H. Pseudopotential approaches to Ca, Sr, and Ba hydrides. Why are some alkaline earth MX₂ compounds bent? *J. Chem. Phys.* **1991**, *94*, 1360–1366.
- (97) Bergner, A.; Dolg, M.; Küchle, W.; Stoll, H.; Preuß, H. Ab initio energy-adjusted pseudopotentials for elements of groups 13–17. *Mol. Phys.* **1993**, *80*, 1431–1441.
- (98) Barone, V.; Cossi, M. Quantum Calculation of Molecular Energies and Energy Gradients in Solution by a Conductor Solvent Model. *J. Phys. Chem. A* **1998**, *102*, 1995–2001.
- (99) Bukowski, M. R.; Comba, P.; Lienke, A.; Limberg, C.; de Laorden, C. L.; Mas-Balleste, R.; Merz, M.; Que, L., Jr. Catalytic Epoxidation and 1,2-Dihydroxylation of Olefins with Bispidine–Iron(II)/H₂O₂ Systems. *Angew. Chem., Int. Ed.* **2006**, *45*, 3446–3449.